

1           **Spurious forces can dominate the vorticity budget of**  
2                                   **ocean gyres on the C-grid**

3           **Andrew F. Styles<sup>1</sup>, Michael J. Bell<sup>2</sup>, David P. Marshall<sup>1</sup>, and David Storkey<sup>2</sup>**

4                                   <sup>1</sup>Department of Physics, University of Oxford, Oxford, UK

5                                   <sup>2</sup>Met Office, Fitzroy Road, Exeter, UK

6           **Key Points:**

- 7           • The vorticity budget is used to identify forces spinning gyres up and down when  
8           integrated over the area enclosed by streamlines  
9           • Spurious topographic forces and a numerical beta effect emerge from the Corio-  
10           lis acceleration when using a C-grid with  $z$ -coordinates  
11           • The identified spurious forces are significant in both an idealized gyre configura-  
12           tion and the Weddell Gyre in a realistic global model

## Abstract

Gyres are prominent surface structures in the global ocean circulation that often interact with the sea floor in a complex manner. Diagnostic methods, such as the depth-integrated vorticity budget, are needed to assess exactly how such model circulations interact with the bathymetry. Terms in the vorticity budget can be integrated over the area enclosed by streamlines to identify forces that spin gyres up and down. In this article we diagnose the depth-integrated vorticity budgets of both idealized gyres and the Weddell Gyre in a realistic global model. It is shown that spurious forces play a significant role in the dynamics of all gyres presented and that they are a direct consequence of the Arakawa C-grid discretization and the  $z$ -coordinate representation of the sea floor. The spurious forces include a numerical beta effect and interactions with the sea floor which originate from the discrete Coriolis force when calculated with the following schemes: the energy conserving scheme (ENE); the enstrophy conserving scheme (ENS); and the energy and enstrophy conserving scheme (EEN). Previous studies have shown that bottom pressure torques provide the main interaction between the depth-integrated flow and the sea floor. Bottom pressure torques are significant, but spurious interactions with bottom topography are similar in size. Possible methods for reducing the identified spurious topographic forces are discussed. Spurious topographic forces can be alleviated by using either a B-grid in the horizontal plane or a terrain-following vertical coordinate.

## Plain Language Summary

Gyres are large scale circulations in the world ocean that often interact with the sea floor. It is important to develop a method to assess how the representation of the sea floor in models affects gyre circulations. By calculating how model forces generate vorticity (the tendency to rotate) in the flow, we are able to determine the forces acting with and against the gyre circulation. We apply this method to results from a simplified double gyre model and the Weddell Gyre in a realistic global model. We show that spurious forces which emerge from the layout of the model grid play an important role in the presented gyre circulations. The spurious forces originate from the calculation of the Coriolis acceleration in the model. In previous studies, it has been argued that gyre circulations interact with the sea floor primarily by forming pressure gradients; here we show that contributions from pressure gradients are significant, but the spurious forces are similar in size and also emerge from interactions with the sea floor. We discuss possible approaches to reduce the identified spurious forces by considering alternative grid layouts. The spurious forces can be alleviated by using a B-grid or a terrain-following vertical coordinate.

## 1 Introduction

Accurately representing the sea floor has always been a challenge for the ocean modelling community. Quantifying the full influence of the sea floor on model circulations is important for both future model development and the interpretation of results from existing models. We present a diagnostic method that reveals how bottom topography influences the depth-integrated vorticity budget of general circulation models (GCMs) and we identify significant spurious forces that emerge from the discrete Coriolis force when calculated on a C-grid (Mesinger & Arakawa, 1976) using  $z$ -coordinates.

The recent article by Stewart et al. (2021) also studied the impact of bottom topography on vorticity budgets. However, the model used by Stewart et al. (2021) is a two layer isopycnal model where the bottom topography is completely contained in the lower density layer. In this article we consider models that have a higher vertical resolution and a step-like bathymetry. It is in these more commonly used models that we identify a new category of spurious forces.

62 The textbook theory of gyres relies on the idea of a depth-integrated vorticity bud-  
 63 get and gyres can be classified by the leading order terms in the depth-integrated vor-  
 64 ticity equation. For example, the Stommel (1948) gyre is dominated by wind stress curl,  
 65 lateral bottom friction, and the beta effect. In another example, Niiler (1966) analyt-  
 66 ically integrated the vorticity equation over the area enclosed by gyre streamlines to study  
 67 inertial gyres dominated by the wind stress curl, the advection of vorticity, and lateral  
 68 bottom friction.

69 GCMs have a primitive momentum equation with an associated vorticity budget.  
 70 By taking the curl of the depth-integrated terms from the primitive momentum equa-  
 71 tion we can calculate the corresponding terms in the model’s depth-integrated vortic-  
 72 ity equation (referred to as vorticity diagnostics hereafter). The vorticity diagnostics can  
 73 then be integrated over the area enclosed by gyre streamlines to reveal the model forces  
 74 responsible for spinning the gyre up and down. In this article we diagnose the vortic-  
 75 ity budget of gyres in two case studies using the NEMO model (Madec et al., 2019). We  
 76 consider a simple double gyre configuration with analytic forcing and idealized geom-  
 77 etry which resembles a North Atlantic basin. We also consider the vorticity budget of  
 78 the Weddell Gyre in a realistic configuration of the global ocean. In both of these case  
 79 studies we identify spurious force profiles with different characteristics. In the light of  
 80 these results, we discuss potential changes to the model discretizations that could miti-  
 81 gate the spurious forces.

82 The article is structured as follows. We first discuss the analytic depth-integrated  
 83 vorticity budget in Section 2 as well as the analytic method of contour integration. In  
 84 Section 3 we consider how the depth-integrated vorticity budget behaves on a C-grid with  
 85 step-like bathymetry and how spurious terms emerge from the discrete Coriolis accel-  
 86 eration. Results from the analytically forced double gyre model are presented in Section  
 87 4 and results for the Weddell Gyre are presented in Section 5. A discussion of approaches  
 88 to avoid the spurious forcing terms can be found in Section 6. Closing remarks are given  
 89 in Section 7. In Appendix A we derive the depth-integrated vorticity equation and in  
 90 Appendix B we present the discrete forms of the Coriolis acceleration for various vor-  
 91 ticity schemes. Appendix C presents results from the double gyre model using various  
 92 forms of the discrete Coriolis acceleration. Appendix D presents contour integrations of  
 93 uninterpolated diagnostics from the double gyre model.

## 94 **2 The analytic vorticity budget**

### 95 **2.1 The depth-integrated vorticity equation**

96 Vorticity diagnostics are an underused tool for interpreting model circulations and  
 97 offer a description of gyre dynamics that complements textbook theory (Vallis, 2017).  
 98 A handful of recent papers have used a vorticity budget to diagnose regional and global  
 99 GCM models (Hughes & de Cuevas, 2001; Yeager, 2015; Schoonover et al., 2016; Le Bras  
 100 et al., 2019; Le Corre et al., 2020).

101 To obtain a depth-integrated vorticity budget analytically we start from the vector-  
 102 invariant form of the momentum equation:

$$103 \quad \frac{\partial \mathbf{u}_h}{\partial t} = - \left[ (\nabla \times \mathbf{u}) \times \mathbf{u} + \frac{1}{2} \nabla (\mathbf{u} \cdot \mathbf{u}) \right]_h - f (\hat{\mathbf{k}} \times \mathbf{u})_h - \frac{1}{\rho_0} \nabla_h P + \mathcal{F}^{\mathbf{u}} + \mathcal{D}^{\mathbf{u}}, \quad (1)$$

104 where  $f$  is the Coriolis parameter,  $\mathcal{F}^{\mathbf{u}}$  is top and bottom surface forcing,  $\mathcal{D}^{\mathbf{u}}$  is the lat-  
 105 eral diffusion of momentum,  $\mathbf{u}_h$  is the ‘horizontal’ (parallel to the Earth’s surface) ve-  
 106 locity vector,  $\nabla_h$  is the horizontal gradient operator, and  $[\cdot]_h$  is the horizontal compo-  
 107 nent of a vector. To derive a depth-integrated vorticity equation, we need to depth-integrate  
 108 and take the curl of Equation 1. The order of the two operations and any multiplications  
 109 carried out significantly alters the form and physical meaning of the obtained depth-integrated  
 110 vorticity equation.

111 If we choose to depth-integrate the curl of the momentum equation, the pressure  
 112 gradient vanishes upon taking the curl and bottom vortex stretching represents the in-  
 113 teraction of the currents with the sea floor. Both the beta effect and bottom vortex stretch-  
 114 ing originate from the Coriolis acceleration in Equation 1. In the model, the curl of the  
 115 single momentum diagnostic associated with the Coriolis acceleration will be responsi-  
 116 ble for two distinct physical processes. Jagannathan et al. (2021) use this form of vorticity  
 117 budget to investigate flow interactions with idealized bathymetry. In Section 6.2  
 118 we discuss whether the spurious forces identified in this article emerge in this vorticity  
 119 budget.

120 If we choose to take the curl of the depth-*averaged* momentum equation then sea  
 121 floor interactions are represented by the JEBAR term (Joint Effect of Baroclinicity and  
 122 Relief). Cane et al. (1998) and Drijfhout et al. (2013) have questioned the relevance of  
 123 JEBAR by presenting simple examples in which there is no flow immediately above the  
 124 bathymetry. In these examples there is trivially no interaction between the flow and the  
 125 bathymetry, but there is a non-zero JEBAR term.

126 Throughout this paper we consider the vorticity equation obtained by taking the  
 127 curl of the depth-integrated momentum equation:

$$\begin{aligned}
 128 \quad \frac{\partial}{\partial t} (\nabla \times \mathbf{U}) \cdot \hat{\mathbf{k}} = & - \underbrace{\nabla_h \cdot (f\mathbf{U})}_{\text{Planetary Vort.}} + \underbrace{\frac{1}{\rho_0} (\nabla P_b \times \nabla H) \cdot \hat{\mathbf{k}}}_{\text{Bottom pressure torque}} + \underbrace{\frac{1}{\rho_0} (\nabla \times \boldsymbol{\tau}_{\text{top}}) \cdot \hat{\mathbf{k}}}_{\text{Surface stress curl}} \\
 129 \quad & - \underbrace{\frac{1}{\rho_0} (\nabla \times \boldsymbol{\tau}_{\text{bot}}) \cdot \hat{\mathbf{k}}}_{\text{Bottom friction}} + \underbrace{\mathcal{D}^\zeta}_{\text{Lateral diffusion}} \\
 130 \quad & - \underbrace{\nabla_h \cdot \left( \int_{-H(x,y)}^{\eta(x,y,t)} \zeta \mathbf{u} dz \right) - \left[ \nabla \times \left( \int_{-H(x,y)}^{\eta(x,y,t)} \frac{1}{2} \nabla_h (\mathbf{u}_h^2) + w \frac{\partial \mathbf{u}_h}{\partial z} dz \right) \right]}_{\text{Advection}} \cdot \hat{\mathbf{k}}. \quad (2)
 \end{aligned}$$

131 Here  $\zeta$  is the vertical component of the vorticity,  $\boldsymbol{\tau}_{\text{top}}$  is the surface stress due to wind  
 132 and sea ice,  $\boldsymbol{\tau}_{\text{bot}}$  is the bottom stress due to friction at the sea floor,  $\mathcal{D}^\zeta$  is the lateral  
 133 diffusion of depth-integrated relative vorticity,  $\eta$  is the free surface height,  $H$  is the depth  
 134 of the sea floor, and  $P_b$  is the pressure at the sea floor. In Equation 2 we omit the con-  
 135 tribution from free surface undulations as we assume the time evolution of the free sur-  
 136 face is small and we omit atmospheric pressure torques as we are assuming there are no  
 137 atmospheric pressure gradients above the ocean. The derivation of Equation 2 (includ-  
 138 ing the omitted terms) is presented in Appendix A.

139 The terms on the right-hand side of Equation 2 are the following: the advection  
 140 of planetary vorticity; the bottom pressure torque; the surface stress curl; the curl of bot-  
 141 tom friction; the lateral diffusion of relative vorticity; and the advection of relative vor-  
 142 ticity. The planetary vorticity term in Equation 2 contains contributions from the evol-  
 143 ving free surface and surface water fluxes as  $\nabla_h \cdot \mathbf{U} = -\partial\eta/\partial t + Q/\rho_0$ , where  $Q$  is the  
 144 surface water flux due to evaporation, precipitation, and run-off. In an equilibrated state,  
 145 the free surface evolution is small and the divergence caused by realistic water fluxes is  
 146 negligible. Hence, we assume  $\nabla_h \cdot (f\mathbf{U}) \approx \beta V$  where  $\beta$  represents the linear variation  
 147 of  $f$  with latitude and  $V$  is the meridional component of the depth-integrated velocity.  
 148 This formulation is practical as topographic interactions emerge from pressure gradients  
 149 in the form of the bottom pressure torque and beta effects emerge from the curl of the  
 150 Coriolis acceleration; the Coriolis acceleration is responsible for one physically meaning-  
 151 ful term in the analytic vorticity budget. Equation 2 is also used in Stewart et al. (2021).

152 Jackson et al. (2006) conclude that the leading order balance between bottom pres-  
 153 sure torques and the planetary vorticity term in Equation 2 is crucial for steering jets  
 154 and western boundary currents over bottom topography. They continue to argue that

155 the form of the topographic steering determines if bottom friction is able to modify the  
 156 geometry of the current.

157 As a consequence of Stokes' theorem, the area integral of a term from Equation 2  
 158 is directly related to the line integral of the depth-integrated forces along the area edge.  
 159 This is particularly useful when considering area integrals of terms from the vorticity equa-  
 160 tion and is discussed further in the next sub-section.

## 161 2.2 Contour integration method

162 All terms in the depth-integrated vorticity equation can be expressed as the curl  
 163 of a depth-integrated acceleration in the momentum equation:

$$\Omega = (\nabla \times \mathbf{M}) \cdot \hat{\mathbf{k}}, \quad (3)$$

164 where  $\Omega$  is a term in the depth-integrated vorticity equation and  $\mathbf{M}$  is a term in the depth-  
 165 integrated momentum equation. If we integrate  $\Omega$  over the area enclosed by a depth-integrated  
 166 streamline, we can interpret the integral using Stokes' theorem:

$$167 \quad I(\psi) = \pm \iint_{A_\psi} \Omega dA = \pm \oint_{\Gamma_\psi} \mathbf{M} \cdot d\mathbf{l}, \quad (4)$$

168 where  $A_\psi$  is the area enclosed by a depth-integrated streamline and  $\Gamma_\psi$  is the anticlock-  
 169 wise path along the same streamline. The criteria for selecting the sign in Equation 4  
 170 is defined later in this paragraph. The depth-integrated stream function,  $\psi$ , only exists  
 171 if the flow is steady and  $\nabla_h \cdot \mathbf{U} = 0$ . If a long time-average of a varying flow is taken  
 172 and the surface water fluxes are sufficiently small, a quasi-streamline can be calculated  
 173 which approximately follows the circulation. The integral  $I(\psi)$  can be interpreted as  
 174 the work done per unit mass by the force associated with  $\mathbf{M}$  on a fluid column in one  
 175 circulation of  $\Gamma_\psi$ . For a gyre circulating in a clockwise direction, the direction of circula-  
 176 tion would be opposite to the conventional anticlockwise direction of  $\Gamma_\psi$ . So that the  
 177 reader does not have to constantly consider the direction of the flow relative to  $\Gamma_\psi$  we  
 178 select the sign in Equation 4 so a positive value of  $I(\psi)$  corresponds to a force that is  
 179 spinning the gyre up.

Analytically, we would expect the planetary vorticity term to vanish upon integra-  
 tion as a consequence of the divergence theorem:

$$\iint_{A_\psi} \nabla_h \cdot (f\mathbf{U}) dA = \oint_{\Gamma_\psi} f\mathbf{U} \cdot \hat{\mathbf{n}} dl = 0, \quad (5)$$

180 where  $\hat{\mathbf{n}}$  is the horizontal vector which is normal to the streamline and the depth-integrated  
 181 velocity. The Coriolis force can still play a role in shaping the streamlines of the circu-  
 182 lation but ultimately has no influence on the integrated budget. Although the divergent  
 183 part of the advection term,  $\nabla_h \cdot (\int \zeta \mathbf{u} dz)$ , has a similar form, we do not expect the same  
 184 zero integral for this term as the depth-integrated product of  $\zeta$  and  $\mathbf{u}$  is not parallel to  
 185  $\mathbf{U}$  in general.

186 This method has been used in models before. Schoonover et al. (2016) integrated  
 187 vorticity diagnostics over a limited number of streamlines in the North Atlantic and con-  
 188 cluded that the wind stress curl is largely balanced by bottom pressure torques. Stewart  
 189 et al. (2021) also used this method in an isopycnal model and concluded that wind stress  
 190 curl is not balanced by bottom pressure torques in general. Stewart et al. (2021) discuss  
 191 how the integrating area affects the resultant vorticity balances and in their model the  
 192 wind stress curl is only balanced by bottom pressure torques when integrated over lat-  
 193 itude bands. Jackson et al. (2006) note that in their idealized models the vorticity in-  
 194 put from bottom friction mostly disappears when integrated over latitude bands but can  
 195 be significant when integrated over the area enclosed by streamlines.

196 In Gula et al. (2015), terms in the barotropic vorticity budget are integrated over  
 197 an entire subdomain covering the South Atlantic Bight to study the interaction between  
 198 the Gulf Stream and the continental shelf. Flow through the boundaries of the nested  
 199 model is permitted so we would not expect the planetary vorticity term to vanish upon  
 200 integration. These integrations show a leading order balance between the planetary vor-  
 201 ticity term and bottom pressure torques and suggest that bottom pressure torques are  
 202 the dominant mechanism for removing the planetary vorticity imported into the subdo-  
 203 main by the Gulf Stream.

204 It should be noted that Schoonover et al. (2016), Stewart et al. (2021), Jackson et  
 205 al. (2006), and Gula et al. (2015) all use a terrain-following coordinate in their models  
 206 but in this article we study the vorticity budget of a  $z$ -coordinate model. In Section 6.4  
 207 we discuss how the vorticity budget can be affected by the choice of vertical coordinate  
 208 and how terrain-following coordinates can mitigate spurious Coriolis forces related to the  
 209 topography.

### 210 3 The vorticity budget on a C-grid

#### 211 3.1 The discrete depth-integrated vorticity equation

212 In many contemporary ocean GCMs, the discretized model variables are distributed  
 213 on the C-grid (Mesinger & Arakawa, 1976). The geometry of the C-grid is shown in Fig-  
 214 ure 1:  $T$  points hold scalar information including the divergence of the flow; the  $U$  and  
 215  $V$  points hold the horizontal components of vector quantities including the horizontal  
 216 velocity, surface stresses, and accelerations in the momentum equation. Values closely  
 217 related to vorticity are found on  $F$  points, this includes the relative vorticity, the stream-  
 218 function, and terms in the depth-integrated vorticity equation ( $\Omega$ ). Vertical velocities  
 219 are located on  $W$  points that are directly above and below  $T$  points as shown in Figure  
 220 1. The Coriolis parameter can be evaluated at any point on the C grid but  $F$  point val-  
 221 ues are used for calculating the Coriolis acceleration in most models that use a vector  
 222 invariant momentum equation because the relative and planetary vorticity are then eval-  
 223 uated at the same point (see Section 3.2). In this article,  $f_{i,j}$  refers to the value of the  
 224 Coriolis parameter centred on the  $F$  point and  $f_{i,j}^u$  ( $f_{i,j}^v$ ) refers to the Coriolis param-  
 225 eter centred on the  $U$  ( $V$ ) point as shown in Figure 1.

226 Every point in the C-grid has an associated cell with a vertical thickness and hor-  
 227 izontal width. Throughout this article  $e^{3t}$  is the  $T$  cell vertical thickness and  $e^{1t}$ ,  $e^{2t}$  are  
 228 the  $T$  cell widths in the  $i$  and  $j$  direction respectively. The same convention is used for  
 229  $U$ ,  $V$ , and  $F$  cells also. It should be noted that the values of the  $F$  cell thicknesses in  
 230 this article depend on the scheme used to calculate the Coriolis acceleration (see Sec-  
 231 tion 3.2).

232 The GCM configurations discussed in this paper use a primitive momentum equa-  
 233 tion that is a discrete equivalent to the vector invariant momentum equation (Madec et  
 234 al., 2019). Momentum diagnostics can be combined to represent terms in the analytic  
 235 momentum equation (Equation 1). The curl of the depth-integrated momentum diag-  
 236 nostics is taken to form a closed discrete vorticity budget that is valid in an unsteady  
 237 state as the time derivative diagnostic is included. The resultant vorticity diagnostics  
 238 should closely resemble the terms in the depth-integrated vorticity equation (Equation  
 239 2); however, the planetary vorticity diagnostic deviates from the planetary vorticity term  
 240 in several significant ways.

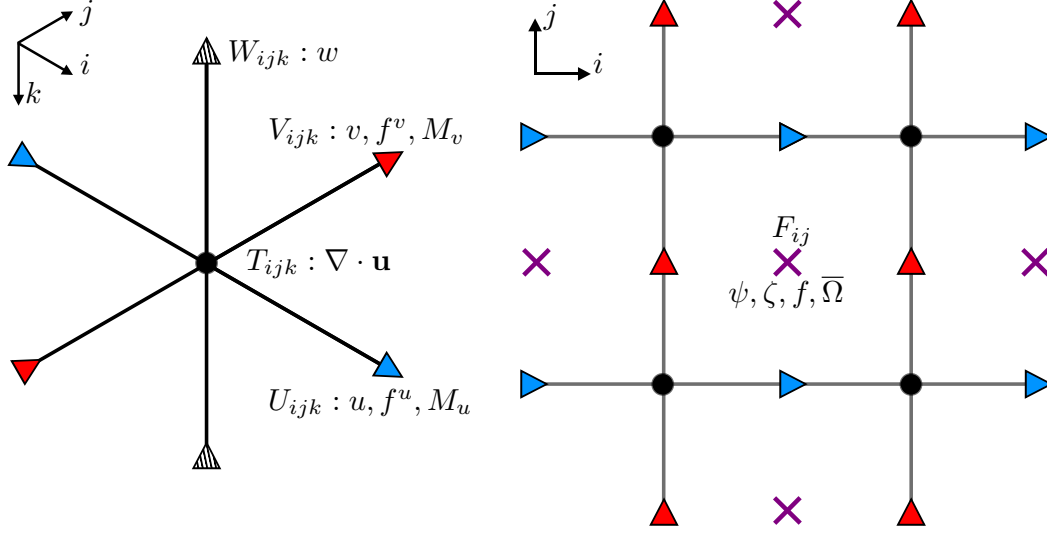


**Figure 1.** The distribution of variables on the C-grid in both a three dimensional (left) and horizontal (right) view. The  $T$ ,  $U$ ,  $V$ ,  $F$ , and  $W$  points are shown alongside important values that are centred on these points. The variable  $w$  is the vertical velocity and  $M_u$ ,  $M_v$  are the  $x$  and  $y$  components of a term in the momentum equation. Note that  $k$  increases downwards.

241

### 3.2 The discrete Coriolis acceleration

242

The Coriolis acceleration is a product of the Coriolis parameter,  $f$ , and the horizontal velocity  $\mathbf{u}_h$ . There are many possible schemes for calculating their product and the choice of scheme affects the quantities that are conserved in the model flow.

243

244

Consider the following discrete Coriolis acceleration:

245

$$\begin{aligned} \text{COR}_{i,j,k}^x &= \frac{1}{4} \frac{1}{(e^{1u}e^{3u})_{i,j,k}} \sum_{n=1}^4 f^v(\mathbf{r}_n) \tilde{V}_k(\mathbf{r}_n), \\ \text{COR}_{i,j,k}^y &= \frac{-1}{4} \frac{1}{(e^{2v}e^{3v})_{i,j,k}} \sum_{n=1}^4 f^u(\mathbf{r}_n) \tilde{U}_k(\mathbf{r}_n), \end{aligned} \quad (6)$$

246

247

248

249

where  $\text{COR}^x$  ( $\text{COR}^y$ ) is the  $x$  ( $y$ ) component of the discrete Coriolis acceleration;  $\tilde{V} = ve^{1v}e^{3v}$  and  $\tilde{U} = ue^{2u}e^{3u}$  are volume fluxes; and  $\mathbf{r}_n$  points to one of the four neighbouring  $V$  or  $U$  points. If we depth-integrate the acceleration in Equation 6 and then take the curl, we obtain the following equation for the discrete planetary vorticity term:

$$\begin{aligned} \text{PVO}_{i,j,k} &= -\frac{1}{4} \frac{1}{(e^{1f}e^{2f})_{i,j}} [(f^u U e^{2u})_{i+1,j} + (f^u e^{2u} U)_{i+1,j+1} \\ &\quad - (f^u U e^{2u})_{i-1,j} - (f^u U e^{2u})_{i-1,j+1} \\ &\quad + (f^v V e^{1v})_{i,j+1} + (f^v V e^{1v})_{i+1,j+1} \\ &\quad - (f^v V e^{1v})_{i,j-1} - (f^v V e^{1v})_{i+1,j-1}], \end{aligned} \quad (7)$$

250

251

252

253

254

255

where PVO is the discrete planetary vorticity term. Equation 7 is the discrete calculation of  $-\nabla_h \cdot (f\mathbf{U})$  averaged over the four  $T$  cells surrounding the central  $F$  point and is therefore closely related to the analytic planetary vorticity term in Equation 2. The Coriolis acceleration given in Equation 6 is not used in C-grid models as it lacks the energy and/or enstrophy conserving properties of other mainstream schemes. However, when studying the discrete depth-integrated vorticity budget it is useful to consider how the

256

used Coriolis accelerations deviate from this reference value as any difference may emerge as a departure from the discrete calculation of  $-\nabla_h \cdot (f\mathbf{U})$  in the vorticity budget.

257

258

When using a vector invariant momentum equation, mainstream schemes use multi-point and thickness-weighted averaging of  $f$  and  $\mathbf{u}$  in order to conserve energy and/or enstrophy (Madec et al., 2019). A general form of the discrete Coriolis acceleration under these schemes is:

259

$$\text{COR}_{i,j,k}^x = \frac{1}{N} \frac{1}{e_{i,j}^{1u}} \sum_{n=1}^N \left( \frac{f(\mathbf{a}_n)}{e_k^3(\mathbf{b}_n)} \right) \tilde{V}_k(\mathbf{c}_n), \quad (8)$$

260

$$\text{COR}_{i,j,k}^y = \frac{-1}{N} \frac{1}{e_{i,j}^{2v}} \sum_{n=1}^N \left( \frac{f(\mathbf{a}_n)}{e_k^3(\mathbf{b}_n)} \right) \tilde{U}_k(\mathbf{c}_n), \quad (9)$$

261

262

where  $\mathbf{a}_n$ ,  $\mathbf{b}_n$ , and  $\mathbf{c}_n$  are the horizontal locations of three neighbouring grid points (not necessarily different) for the  $n^{\text{th}}$  term of the sum. Note that  $\mathbf{a}_n$  is always the location of an  $F$  point and  $\mathbf{c}_n$  is always the location of a  $U$  or  $V$  point. Depending on the scheme, the  $e_k^3$  term can be either a  $U$ ,  $V$ , or  $F$  cell thickness so  $\mathbf{b}_n$  is the location of either a  $U$ ,  $V$ , or  $F$  point.  $N$  is the number of terms in the average which depends on the choice of scheme. Equations 8 and 9 are valid on points near the bathymetry but if  $\mathbf{b}_n$  or  $\mathbf{c}_n$  points to a masked grid point (a point in the bathymetry) then the  $n^{\text{th}}$  term in the sum is equal to zero.

263

264

265

266

267

268

269

270

In this article we consider three popular schemes for calculating the Coriolis acceleration. The energy conserving scheme (ENE) (Sadourny, 1975) conserves total horizontal kinetic energy and uses a four point average ( $N=4$ ). The enstrophy conserving scheme (ENS) (Sadourny, 1975) conserves potential enstrophy and has eight terms ( $N=8$ ). Finally the energy and enstrophy conserving scheme (EEN) (Arakawa & Lamb, 1981) conserves both horizontal kinetic energy and potential enstrophy and uses a twelve point average ( $N=12$ ). Barnier et al. (2006) demonstrates that the choice of scheme can significantly influence the global ocean circulation, especially in areas with strong current-topography interaction.

271

272

273

274

275

276

277

278

279

The explicit forms of the ENE, ENS, and EEN schemes for the Coriolis acceleration are given in Appendix B. The results in Section 4 and 5 use the EEN scheme; however, in Section 6.1 we argue that all three schemes produce similar spurious forces. This argument is more concise when we use a form of the Coriolis acceleration that is general to the ENE, ENS, and EEN schemes.

280

281

282

283

284

We will decompose the general discrete Coriolis acceleration in Equation 6 by considering variations of  $f$  and  $e^3$  around the  $U$  and  $V$  points:

285

286

$$f(\mathbf{a}_n) = f(\mathbf{c}_n) + [f(\mathbf{a}_n) - f(\mathbf{c}_n)], \quad (10)$$

287

$$e_k^3(\mathbf{b}_n) = \frac{1}{\alpha_k(\mathbf{b}_n)} (e_{i,j,k}^{3u} + [\alpha_k(\mathbf{b}_n)e_k^3(\mathbf{b}_n) - e_{i,j,k}^{3u}]), \quad (11)$$

288

$$e_k^3(\mathbf{b}_n) = \frac{1}{\alpha_k(\mathbf{b}_n)} (e_{i,j,k}^{3v} + [\alpha_k(\mathbf{b}_n)e_k^3(\mathbf{b}_n) - e_{i,j,k}^{3v}]), \quad (12)$$

289

where  $f(\mathbf{c}_n)$  is the value of the Coriolis parameter centred on the same point as the volume flux. Equation 11 will be applied to  $\text{COR}^x$  (Equation 8) and Equation 12 will be applied to  $\text{COR}^y$  (Equation 9). The  $\alpha_k(\mathbf{b}_n)$  term is of order one and represents the scaling of  $e_k^3$  relative to other local cell thicknesses that only occurs in the EEN scheme. In the EEN scheme,  $e_k^3(\mathbf{b}_n)$  is an  $F$  cell thickness and  $F$  cell thicknesses are calculated using:

290

291

292

293

294

295

$$e_{i,j,k}^{3f} = \frac{1}{4} (e_{i,j,k}^{3t} + e_{i+1,j,k}^{3t} + e_{i,j+1,k}^{3t} + e_{i+1,j+1,k}^{3t}), \quad (13)$$

296

where masked  $T$  cell thicknesses are set to zero. When near bathymetry (masked points), the  $F$  cell thickness could be up to four times smaller than the typical unmasked  $T$  cell

297

298 thicknesses surrounding it. The product  $\alpha_k e_k^{3f}$  is the  $F$  cell thickness before this scal-  
 299 ing is applied and will be more similar to the neighbouring  $T$  cell thicknesses in Equa-  
 300 tion 13. This scaling of  $e^{3f}$  is unique to the EEN scheme and therefore  $\alpha_k = 1$  in the  
 301 ENS and ENE cases.

302 By combining Equations 8, 9, 10, 11, and 12 we can derive a general decomposi-  
 303 tion of the Coriolis acceleration:

$$\begin{aligned}
 \text{COR}_{i,j,k}^x &= \frac{1}{N} \frac{1}{(e^{1u} e^{3u})_{i,j,k}} \sum_{n=1}^N f(\mathbf{c}_n) \tilde{V}_k(\mathbf{c}_n) \left[ 1 + \underbrace{\frac{f(\mathbf{a}_n) - f(\mathbf{c}_n)}{f(\mathbf{c}_n)}}_{f \text{ displacement}} \right] \\
 &+ \underbrace{\alpha_k(\mathbf{b}_n) \frac{\alpha_k(\mathbf{b}_n) e_k^3(\mathbf{b}_n) - e_{i,j,k}^{3u}}{e_{i,j,k}^{3u}}}_{\text{Cell thicknesses}} + [\alpha_k(\mathbf{b}_n) - 1] + \underbrace{[\alpha_k(\mathbf{b}_n) - 1] \frac{f(\mathbf{a}_n) - f(\mathbf{c}_n)}{f(\mathbf{c}_n)}}_{\text{Coupled } f\text{-topographic}}, \\
 \text{COR}_{i,j,k}^y &= \frac{-1}{N} \frac{1}{(e^{2v} e^{3v})_{i,j,k}} \sum_{n=1}^N f(\mathbf{c}_n) \tilde{U}_k(\mathbf{c}_n) \left[ 1 + \underbrace{\frac{f(\mathbf{a}_n) - f(\mathbf{c}_n)}{f(\mathbf{c}_n)}}_{f \text{ displacement}} \right] \\
 &+ \underbrace{\alpha_k(\mathbf{b}_n) \frac{\alpha_k(\mathbf{b}_n) e_k^3(\mathbf{b}_n) - e_{i,j,k}^{3v}}{e_{i,j,k}^{3v}}}_{\text{Cell thicknesses}} + [\alpha_k(\mathbf{b}_n) - 1] + \underbrace{[\alpha_k(\mathbf{b}_n) - 1] \frac{f(\mathbf{a}_n) - f(\mathbf{c}_n)}{f(\mathbf{c}_n)}}_{\text{Coupled } f\text{-topographic}}, \quad (14)
 \end{aligned}$$

304 where we have assumed that variations in  $f$  and the nonscaled cell thickness,  $\alpha_k e_k^3$ , are  
 305 small. The  $x$  and  $y$  components of the Coriolis acceleration have a leading order contri-  
 306 bution centred on the  $U$  and  $V$  point. The leading order term simplifies to the reference  
 307 Coriolis acceleration in Equation 6 and therefore will resemble  $-\nabla_h \cdot (f\mathbf{U})$  in the dis-  
 308 crete vorticity budget. Equation 14 is valid on points near the bathymetry but if  $\mathbf{b}_n$  or  
 309  $\mathbf{c}_n$  points to a masked grid point then the  $n^{\text{th}}$  term of the entire sum is equal to zero.

310 The remaining terms may emerge as first order departures from  $-\nabla_h \cdot (f\mathbf{U})$  in the  
 311 discrete vorticity budget. The first order contributions are: an  $f$  displacement term caused  
 312 by the difference between the values of  $f$  where the volume fluxes are located and the  
 313 values of  $f$  used in the scheme; a topographic effect caused by variations in cell thick-  
 314 nesses; and a coupled  $f$ -topographic effect caused by the combined effect of sudden changes  
 315 in cell thicknesses near masked points and the previously mentioned  $f$  displacement term.  
 316 Note that if  $\alpha = 1$  (true for ENS and ENE) then the  $f$ -topographic effect vanishes.

317 The depth-integrated Coriolis acceleration is:

$$\begin{aligned}
 \widehat{\text{COR}}_{i,j}^x &= \sum_{k=1}^{k_{\max}^x(i,j)} e_{i,j,k}^{3u} \text{COR}_{i,j,k}^x, \\
 \widehat{\text{COR}}_{i,j}^y &= \sum_{k=1}^{k_{\max}^y(i,j)} e_{i,j,k}^{3v} \text{COR}_{i,j,k}^y, \quad (15)
 \end{aligned}$$

320 where  $k_{\max}^x$  and  $k_{\max}^y$  are the highest unmasked indices in the column and they may vary  
 321 with horizontal index when  $z$ -coordinates are used. The depth-integrated Coriolis ac-  
 322 celeration is therefore also sensitive to steps in the bathymetry. This is discussed in the  
 323 next sub-section.

### 324 3.3 The influence of model level steps on the Coriolis acceleration

325 In this section, we present a toy configuration that highlights how model levels can  
 326 influence the discrete Coriolis acceleration. The configuration is shown in Figure 2. The  
 327 configuration has two model levels, three  $U$ -grid points in the  $i$  direction, two in the  $j$   
 328 direction, and a rigid lid. The points in the upper level are surrounded by unmasked points,

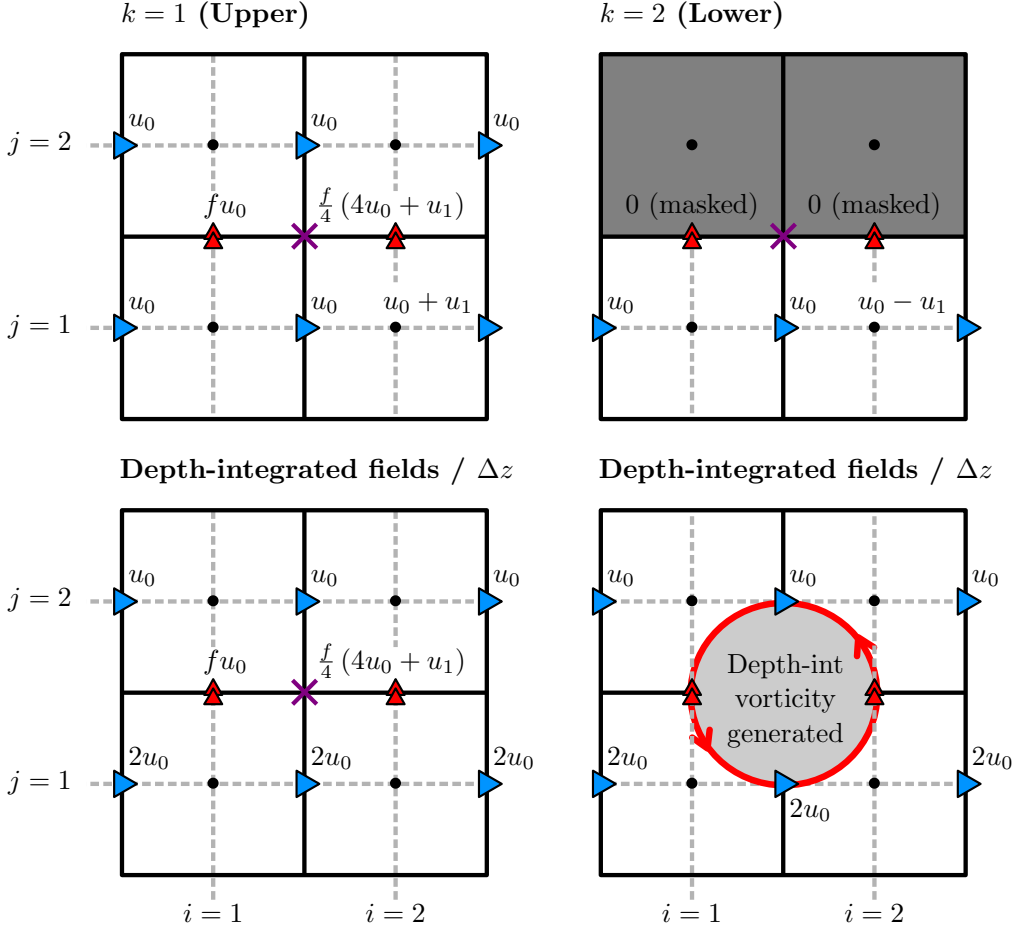


**Figure 2.** A toy model demonstrating how model levels influence the discrete Coriolis acceleration. A horizontal plan is shown for the upper and lower level as well as a view of the depth-integrated fields divided by the cell thickness  $\Delta z$ . Single arrows represent prescribed velocities; double arrows represent calculated Coriolis accelerations; and shaded cells represent bottom topography. Accelerations on the lower level are masked to prevent the velocity field from evolving into a flow that would violate the no penetration boundary condition. The central F point is marked by a cross and is where the depth-integrated vorticity is generated.

329 we assume the grid is regular, and cell widths are the same in the  $i$  and  $j$  direction. We  
 330 also assume an  $f$ -plane so  $f$  does not vary.

331 The configuration has a step bathymetry and a current running alongside it. The  
 332 current has no  $y$  component so  $v = 0$  everywhere and therefore  $\text{COR}^x = 0$  at all points.  
 333 The lower limb of the current decelerates by an amount  $u_1$  and as a consequence of in-  
 334 compressibility a vertical velocity is induced which accelerates the upper current by  $u_1$ .

335 Under these assumptions, the discrete Coriolis acceleration does not vary between  
 336 the ENE, ENS, and EEN schemes and is:

$$337 \quad \text{COR}_{i,j,k}^y = \frac{f}{4} [u_{i,j,k} + u_{i-1,j,k} + u_{i,j+1,k} + u_{i-1,j+1,k}], \quad (16)$$

338 which is effectively  $f$  multiplied by the four point average of  $u$ .

339 In the upper layer, the Coriolis accelerations, located on the  $V$  points marked by  
 340 red triangles in Figure 2, are:

$$341 \quad \text{COR}_{1,1,k=1}^y = fu_0, \quad (17)$$

$$342 \quad \text{COR}_{2,1,k=1}^y = \frac{f}{4}(4u_0 + u_1). \quad (18)$$

343 In the lower layer, the Coriolis accelerations are set to zero as they lie on masked  $V$  points.  
 344 The  $V$  points are masked to prevent accelerations into the topography that would vi-  
 345 olate the no penetration boundary condition. The depth-integrated Coriolis accelerations  
 346 are:

$$347 \quad \widehat{\text{COR}}_{1,1}^y = \text{COR}_{1,1,k=1}^y \Delta z, \quad (19)$$

$$348 \quad \widehat{\text{COR}}_{2,1}^y = \text{COR}_{2,1,k=1}^y \Delta z, \quad (20)$$

349 where  $\Delta z$  is the constant cell thickness. It should be noted that  $u_1$  vanishes when cal-  
 350 culating the depth-integrated velocities but remains in the depth-integrated acceleration.  
 351 The depth-integrated Coriolis acceleration depends on more than the depth-integrated  
 352 velocities.

353 When we take the curl of the depth-integrated accelerations, we can see how a depth-  
 354 integrated vorticity is generated:

$$355 \quad \frac{1}{\Delta x} \left[ \widehat{\text{COR}}_{2,1}^y - \widehat{\text{COR}}_{1,1}^y \right] = \frac{1}{4} \frac{\Delta z}{\Delta x} f u_1, \quad (21)$$

356 where  $\Delta x$  is the constant cell width. Note that this value is located on the central  $F$  point  
 357 shown in Figure 2.

358 The pressure gradient, lateral diffusion term (unless no-slip boundary conditions  
 359 are used), and the horizontal advection term are ambiguous on the  $V$  velocity points at  
 360 masked points on the edge of the bathymetry (e.g. the  $V$  points in the upper right di-  
 361 agram of Figure 2). An explicit momentum balance cannot be resolved and the Cori-  
 362 olis acceleration is the only non-zero and unambiguous acceleration into the sea floor.  
 363 There should be no net acceleration into the bathymetry or else the no penetration bound-  
 364 ary condition would be violated, so all accelerations that are incident on bathymetry are  
 365 masked and set to zero. The masking of all accelerations can be interpreted as the ad-  
 366 dition of a spurious term to the discrete Coriolis acceleration. This spurious force is of  
 367 unclear physical origin and is not realistic as it is localized to grid points that lie near  
 368 model level steps. We can think of the result in Equation 21 as either the curl of this  
 369 spurious force or as a form of spurious vortex stretching that takes place on  $F$  points near  
 370 model level steps (cf. Bell, 1999).

### 371 **3.4 Decomposing the planetary vorticity term**

372 In Section 3.2 we concluded that the discrete Coriolis acceleration used in main-  
 373 stream schemes contained spurious contributions caused by  $f$  displacement, variations  
 374 in cell thicknesses, and a coupled  $f$ -topographic effect. In Section 3.3 we demonstrated  
 375 how spurious contributions from model level steps exist in the depth-integrated discrete  
 376 Coriolis acceleration. The four found spurious contributions have the potential to emerge  
 377 in the planetary vorticity diagnostic which is calculated by taking the curl of the depth-  
 378 integrated Coriolis acceleration:

$$\text{PVO}_{i,j} = \frac{1}{(e^{1f} e^{2f})_{i,j}} \left[ \left( \widehat{\text{COR}}^y e^{2v} \right)_{i+1,j} - \left( \widehat{\text{COR}}^y e^{2v} \right)_{i,j} \right. \\ \left. - \left( \widehat{\text{COR}}^x e^{1u} \right)_{i,j+1} + \left( \widehat{\text{COR}}^x e^{1u} \right)_{i,j} \right]. \quad (22)$$

**Table 1.** The five different calculations of the planetary vorticity term and the components from Equation 23 they include. FD =  $f$  displacement term, E3 = Cell thicknesses term, FT =  $f$ -topographic term, MLV = Model levels steps term.

Calculation	$-\nabla_h \cdot (f\bar{\mathbf{u}})$	FD	E3	FT	MLV
Full diagnostic	✓	✓	✓	✓	✓
Assume $f(\mathbf{a}_n) = f(\mathbf{c}_n)$ , $e^3 = \text{const}$	✓	✗	✗	✗	✓
Assume $e^3 = \text{const}$	✓	✓	✗	✗	✓
Assume $f(\mathbf{a}_n) = f(\mathbf{c}_n)$	✓	✗	✓	✗	✓
Calculate $-\nabla_h \cdot (f\mathbf{U})$	✓	✗	✗	✗	✗

379

380 We can therefore express the planetary vorticity diagnostic as the sum of five com-  
 381 ponents:

$$\begin{aligned}
 \text{PVO}_{i,j} = & -\nabla_h \cdot (f\mathbf{U})|_{i,j} + f \text{ displacement} + \text{cell thicknesses} \\
 & + f\text{-topographic} + \text{model level steps}
 \end{aligned}
 \tag{23}$$

382 where  $-\nabla_h \cdot (f\mathbf{U})|_{i,j}$  refers to the discrete divergence calculation in Equation 7 and  
 383 is closely related to the analytic planetary vorticity term in Equation 2. The remaining  
 384 terms are departures from the analytic estimate that emerge from using mainstream schemes  
 385 to calculate the Coriolis acceleration and the masking of velocity points near the bathymetry.  
 386  
 387

388 The magnitude of these contributions may vary significantly between configurations  
 389 so a general method for decomposing the planetary vorticity diagnostic is valuable. In  
 390 order to calculate the decomposition of the planetary vorticity diagnostic, we calculate  
 391 the Coriolis acceleration under three different assumptions and then calculate the cor-  
 392 responding contributions to the vorticity budget. An explicit calculation of  $-\nabla_h \cdot (f\mathbf{U})|_{i,j}$   
 393 (Equation 7) is also needed. The calculations are listed in Table 1 along with the com-  
 394 ponents from Equation 23 they include. By linearly combining the fields from each cal-  
 395 culation we can isolate each component in Equation 23. The  $f$ -topographic component  
 396 is calculated by finding the difference between the complete planetary vorticity diagnos-  
 397 tic and the sum of the four other components; therefore the five components add up to  
 398 the complete planetary vorticity diagnostic by construction.

### 399 3.5 Contour integration on a C-grid

400 Calculating the curl on a C-grid is consistent with Stokes' law applied to an  $F$  cell,  
 401 and integrating  $\nabla \times \mathbf{M} \cdot \mathbf{k}$  over several adjacent  $F$  cells is equivalent to a line integral  
 402 of  $\mathbf{M}$  around them (see Figure 3). As the streamfunction,  $\psi$ , is defined on  $F$  points we  
 403 can approximate that the area enclosed by a streamline is a collection of interior  $F$  cells  
 404 and that the area integral of vorticity diagnostics is the work done by model forces in  
 405 one circulation around them. This is an approximation as we are assuming that the stream-  
 406 line follows the rectangular edges of the interior  $F$  cells but the resultant error is min-  
 407 imised if we first interpolate the points onto a sufficiently fine grid. The asymptotic value  
 408 the contour integral tends towards as the interpolation resolution is increased should be  
 409 free of area error. This method is applied to all contour integrals presented in Sections  
 410 4 and 5. Any non-topographic contributions to the contour integral that remains after  
 411 the interpolation will be described as a numerical beta effect.

412 A numerical beta effect can emerge from  $-\nabla_h \cdot (f\mathbf{U})|_{i,j}$  even after being inter-  
 413 polated onto a fine grid as the divergence is calculated over the four  $T$  cells that surround  
 414 the central  $F$  point (see Equation 7). When the internal  $F$  points are summed within

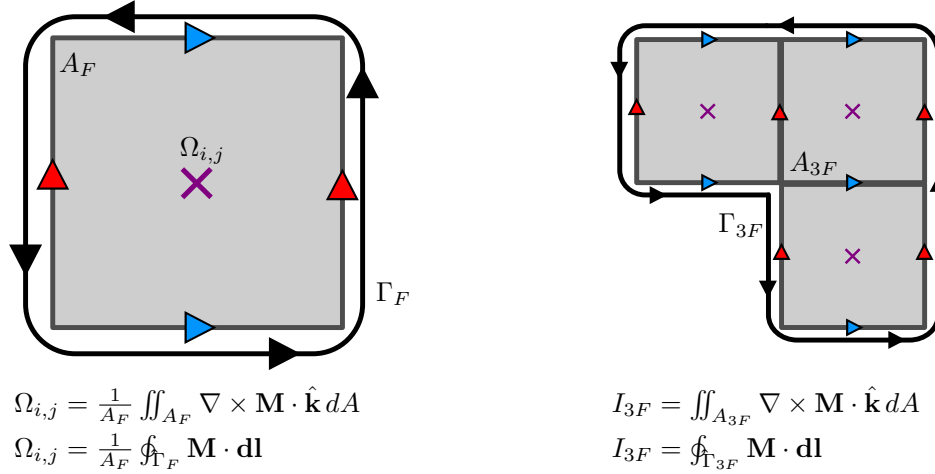


**Figure 3.** The application of Stokes' theorem on a C-grid. The vorticity diagnostic  $\Omega$  is equivalent to the normalized line integral of  $\mathbf{M}$  around a single  $F$  cell of area  $A_F$ . The area integral of  $\Omega$  over a collection of  $F$  cells (e.g.  $A_{3F}$ ) is equivalent to the line integral of  $\mathbf{M}$  along the perimeter (e.g.  $\Gamma_{3F}$ ).

415 the contour, the local domains for calculating the grid point divergences will overlap mean-  
 416 ing the resultant area integral will not satisfy the divergence theorem in general.

## 417 4 A double gyre model

### 418 4.1 Details of the configuration

419 The first experiment in this article is an idealized double gyre configuration based  
 420 on the GYRE PISCES reference configuration in NEMO. The GYRE PISCES reference  
 421 configuration has been used for a wide range of experiments (Lévy et al., 2010, 2015; Rug-  
 422 giero et al., 2015; Perezhogin, 2019). The domain is a closed rectangular basin which is  
 423 3180 km long, 2120 km wide, and is rotated at an angle of  $45^\circ$  relative to the zonal di-  
 424 rection. The basin exists on a beta plane where  $f$  varies linearly around its value at  $\sim$   
 425  $30^\circ\text{N}$ .

426 The model has a regular  $122 \times 82$  grid that is aligned with the rotated basin. The  
 427 horizontal resolution is equivalent to a  $1/4^\circ$  grid at the equator and the configuration has  
 428 31 model levels. Two forms of bathymetry are used in this section. The FLAT config-  
 429 uration has a fixed depth of 4.5km and no partial cells are used. The SLOPED config-  
 430 uration has a linear slope that extends from the North West side of the basin and spans  
 431 half the basin (see Figure 4a). The maximum depth of the SLOPED configuration is 4.5km,  
 432 the minimum depth is 2km, and partial cells are used to represent the slope.

433 The circulation is forced by sinusoidal analytic profiles of surface wind stress and  
 434 buoyancy forcing. The wind stress is zonal and only varies with latitude so that the curl  
 435 changes sign at  $22^\circ\text{N}$  and  $36^\circ\text{N}$  (see Figure 4b). The wind stress profile is designed to spin  
 436 up a subpolar gyre in the north, a subtropical gyre in the south, and a small recircula-  
 437 tion also emerges in the bottom corner. The net surface heat flux takes the form of a restor-  
 438 ing to a prescribed apparent temperature. Further details about the buoyancy forcing  
 439 can be found in Lévy et al. (2010). The wind stress and buoyancy forcing varies season-  
 440 ally in a sinusoidal manner.

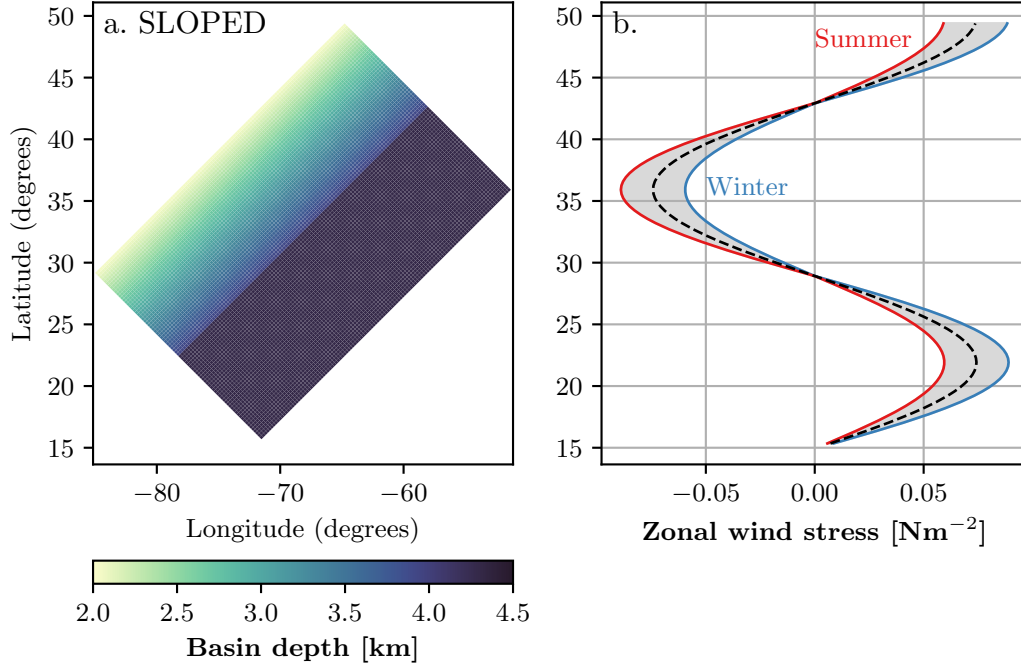


**Figure 4.** (a) Bathymetry of the SLOPED configuration. (b) The wind stress profile for both the FLAT and SLOPED configuration. The wind stress profile varies seasonally in a sinusoidal manner between summer and winter extremes that are highlighted.

441 The model uses a free slip condition on all boundaries except at the bottom where  
 442 a linear friction drag is applied. A simplified linear equation of state is used with a thermal  
 443 expansion coefficient of  $a_0 = 2 \times 10^{-4} \text{kg m}^{-3} \text{K}^{-1}$ , and a haline coefficient of  $b_0 =$   
 444  $7.7 \times 10^{-4} \text{kg m}^{-3} \text{psu}^{-1}$ . Horizontal and biharmonic diffusion of momentum is imple-  
 445 mented with a diffusivity of  $5 \times 10^{10} \text{m}^4 \text{s}^{-1}$ . Biharmonic diffusion of tracers along isopy-  
 446 cnals is implemented with a diffusivity of  $10^9 \text{m}^4 \text{s}^{-1}$ .

447 The model is spun up for 60 years and the experiment was run for an additional  
 448 10 years with monthly-mean outputs. A steady state is not required for the diagnostics  
 449 to be valid as the time derivative term is present in the vorticity budget. A time step  
 450 of 10 minutes is used for the model integration.

451 The EEN vorticity scheme is used for consistency with all analysis discussed in Sec-  
 452 tion 3 and the results from the Weddell Gyre in Section 5. The EEN method calculates  
 453  $F$  cell thicknesses using the method described by Equation 13 and we therefore expect  
 454 sudden changes in the  $F$  cell thickness near the domain edge for both the FLAT and SLOPED  
 455 configurations.

## 456 4.2 Methods

457 Momentum diagnostics are calculated for every time step and the discrete vortic-  
 458 ity diagnostics are calculated by depth-integrating the momentum diagnostics and tak-  
 459 ing the curl. The resultant diagnostics are time-averaged over the ten year experimen-  
 460 tal period. The extensive time-averaging will influence the advection vorticity diagnos-  
 461 tic as there is an added contribution from the eddy vorticity flux.

462 For contour integration, the vorticity diagnostics and depth-integrated stream func-  
 463 tion are then linearly interpolated onto a regular  $1/12^\circ$  grid. This is to minimise errors  
 464 caused by the difference between the true enclosed streamline area and the total area  
 465 of the enclosed  $F$  cells. Interpolation beyond  $1/12^\circ$  resolution makes little difference to  
 466 the results, suggesting that the area error has been significantly suppressed.

467 For 1001 values of  $\psi$ , closed streamline contours are identified using a marching squares  
 468 algorithm from the scikit-image package (Van Der Walt et al., 2014). Streamlines that  
 469 are near the recirculation gyre (south of  $20^\circ\text{N}$ ) are ignored in this experiment and for some  
 470 values of  $\psi$  no closed streamlines could be found. For each closed streamline found, the  
 471 vorticity diagnostics are integrated over the area enclosed; this is equivalent to calculat-  
 472 ing  $I(\psi)$  in Equation 4 over many values of  $\psi$ . The freshwater fluxes mean that  $\nabla_h \cdot \mathbf{U} \neq$   
 473 0 even in a steady state and an exact stream function cannot be calculated. To test how  
 474 closely the calculated streamlines follow the circulation we integrate the positive quan-  
 475 tity  $|f_0(\nabla_h \cdot \mathbf{U})|$  over the same enclosed areas to estimate the magnitude of the er-  
 476 ror caused by the divergent flow. The maximum value of  $f$  is used as  $f_0$  and the largest  
 477 contour integral of  $|f_0(\nabla_h \cdot \mathbf{U})|$  is 0.16 Sv/day which is substantially smaller than the  
 478 leading contour integrals presented in the next sub-section. In addition to this test we  
 479 used an elliptical solver to decompose the depth-integrated flow into compressible and  
 480 incompressible parts; using the streamlines from the incompressible component does not  
 481 change the results presented in the next sub-section.

482 Multiple closed contours can be found for the same value of  $\psi$  so an additional con-  
 483 tour constraint is needed to ensure  $I(\psi)$  is single-valued. In this experiment we always  
 484 choose the contour that spans the largest area which minimises the influence of small  
 485 pocket circulations that are not a part of the gyre. Closed streamlines that run along  
 486 the edge of the domain can be hard to identify so a discontinuity in  $I(\psi)$  near  $\psi = 0$   
 487 is expected as the largest detected contours will suddenly become pocket circulations as  
 488  $\psi$  approaches zero.

### 489 4.3 Results

490 The depth-integrated streamfunction from the FLAT and SLOPED configurations  
 491 is shown in Figure 5. The vorticity of the depth-integrated velocity field is shown in Fig-  
 492 ure 6. In both configurations a subtropical and subpolar gyre can clearly be identified  
 493 and a small recirculation gyre can be found in the Southernmost corner. The subtrop-  
 494 ical gyre circulation is clockwise and the subpolar gyre circulation is anticlockwise.

495 In the FLAT configuration the subtropical gyre has a transport of 65 Sv and the  
 496 subpolar gyre has a transport of 18 Sv. In the SLOPED configuration the subtropical  
 497 gyre has a transport of 38 Sv and the subpolar gyre has a transport of 14 Sv. We note  
 498 that the sloped bathymetry significantly alters the form of the subtropical gyre stream-  
 499 lines.

500 The depth-integrated vorticity diagnostics of the FLAT and SLOPED configura-  
 501 tion are shown in Figures 7 and 8 respectively alongside the decomposition of the plan-  
 502 etary vorticity diagnostic introduced in Section 3.4. In the FLAT configuration we note  
 503 that the non-linear advection of vorticity and the planetary vorticity diagnostic have the  
 504 largest grid point values ( $\sim 10^{-9} \text{ m s}^{-2}$ ) near the western boundary currents of both  
 505 gyres. The wind stress curl is one order of magnitude smaller ( $\sim 10^{-10} \text{ m s}^{-2}$ ) but changes  
 506 sign less frequently within the gyre regions. We see that the planetary vorticity diagnos-  
 507 tic is almost entirely a result of the beta effect (Figure 7g and h). We note that the con-  
 508 tribution from varying cell thicknesses in the FLAT configuration is non-zero and local-  
 509 ized to the edge (Figure 7j) where the EEN Coriolis scheme artificially shrinks  $F$  cell thick-  
 510 nesses near masked points.

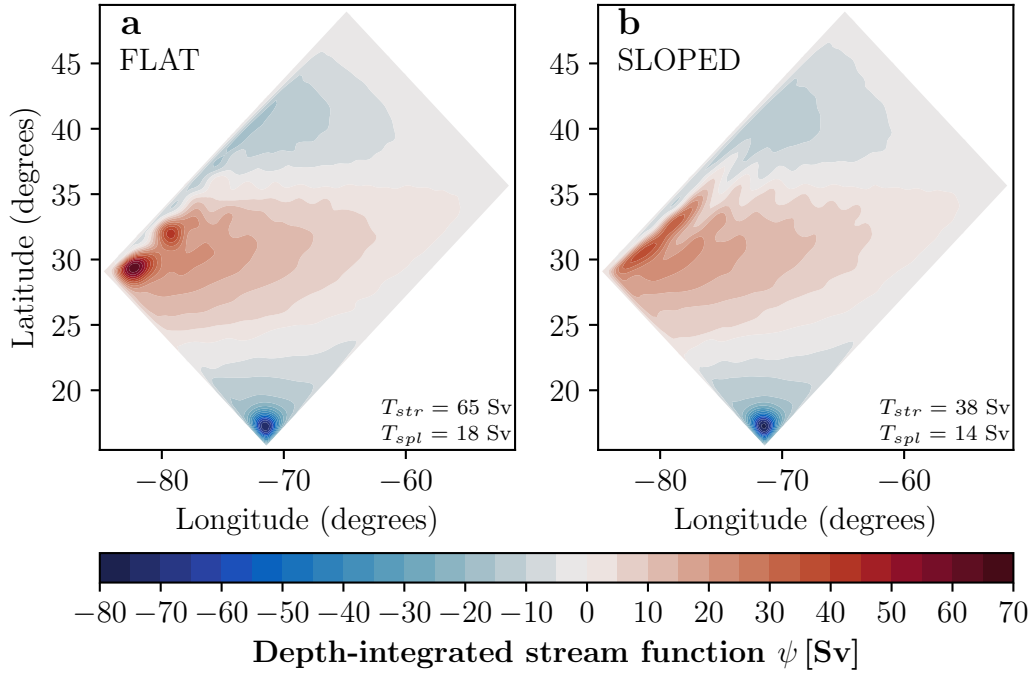


**Figure 5.** The depth-integrated streamfunction (time-averaged) of the (a) FLAT and (b) SLOPED configurations. The transports of the subtropical gyre ( $T_{str}$ ) and subpolar gyre ( $T_{spl}$ ) are given.

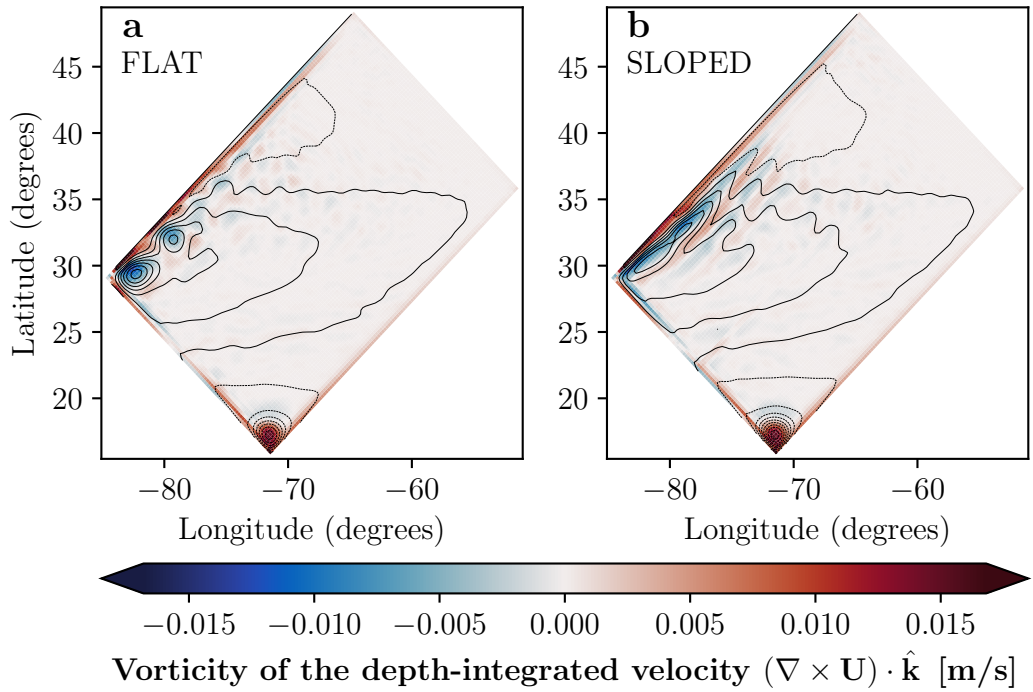


**Figure 6.** The vorticity of the depth-integrated velocity field (time-averaged) for the (a) FLAT and (b) SLOPED configurations. The black contours are streamlines from Figure 5.

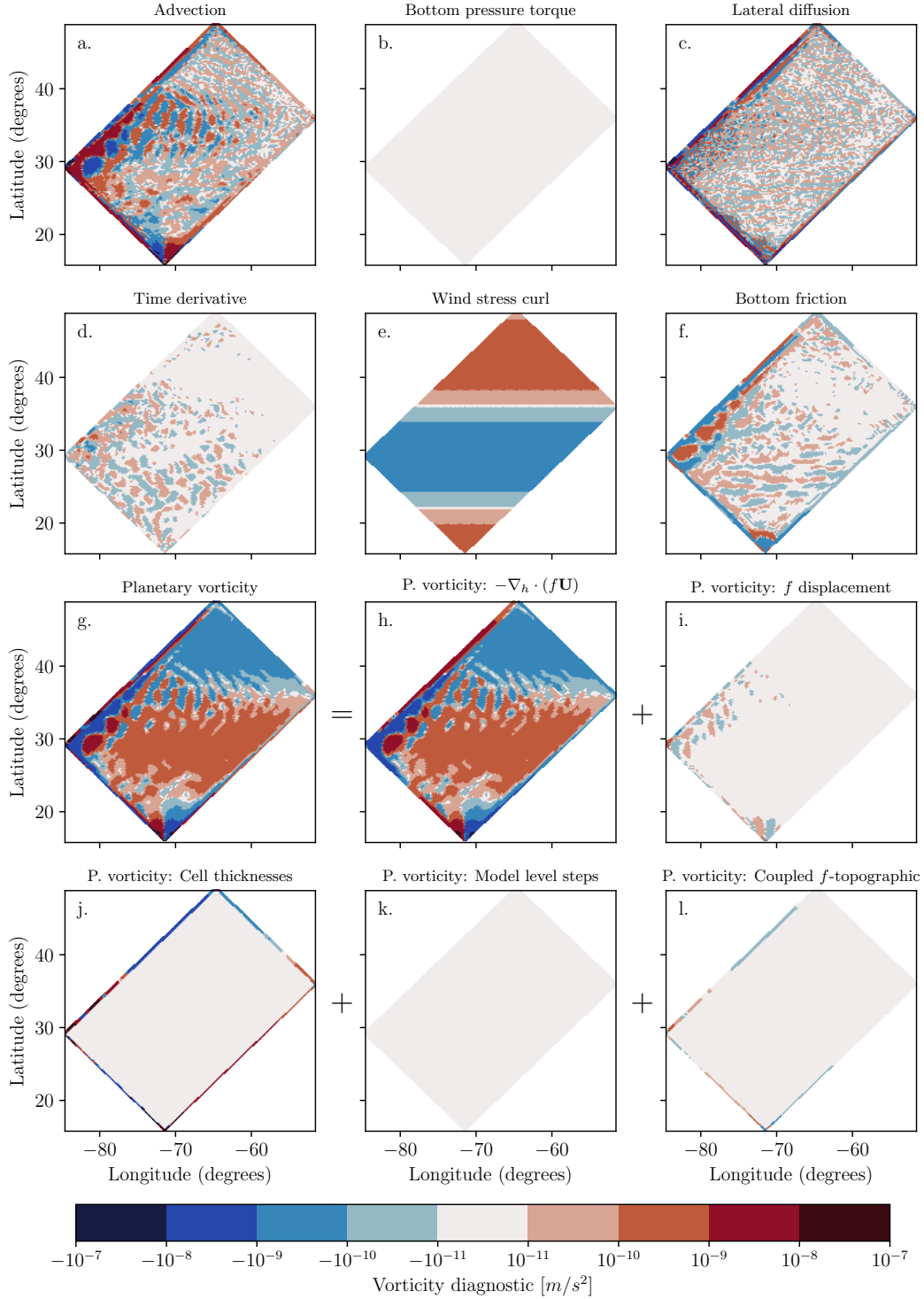


**Figure 7.** The depth-integrated vorticity diagnostics for the FLAT configuration and the components of the planetary vorticity diagnostic (time-averaged). Panels (a) through to (g) are the diagnostics for the terms in the depth-integrated vorticity equation (Equation 2). Panels (h) through to (l) are the components of the planetary vorticity diagnostic in Equation 23 and discussed in Section 3.4. The color bar is logarithmic (for values greater than  $10^{-11}$  in magnitude) and shows the four leading order magnitudes that are positive and negative.

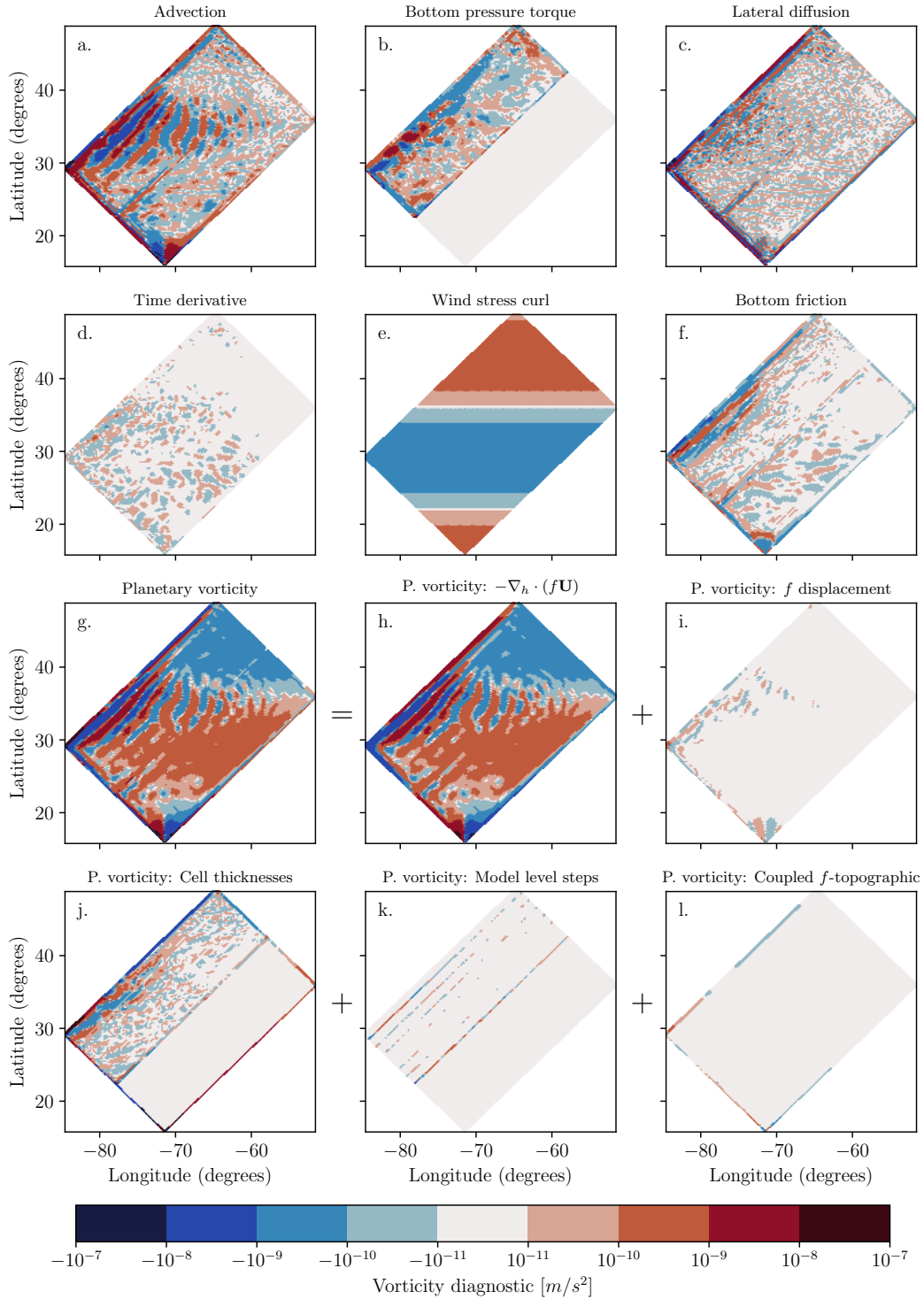


**Figure 8.** The depth-integrated vorticity diagnostics for the SLOPED configuration and the components of the planetary vorticity diagnostic (time-averaged).

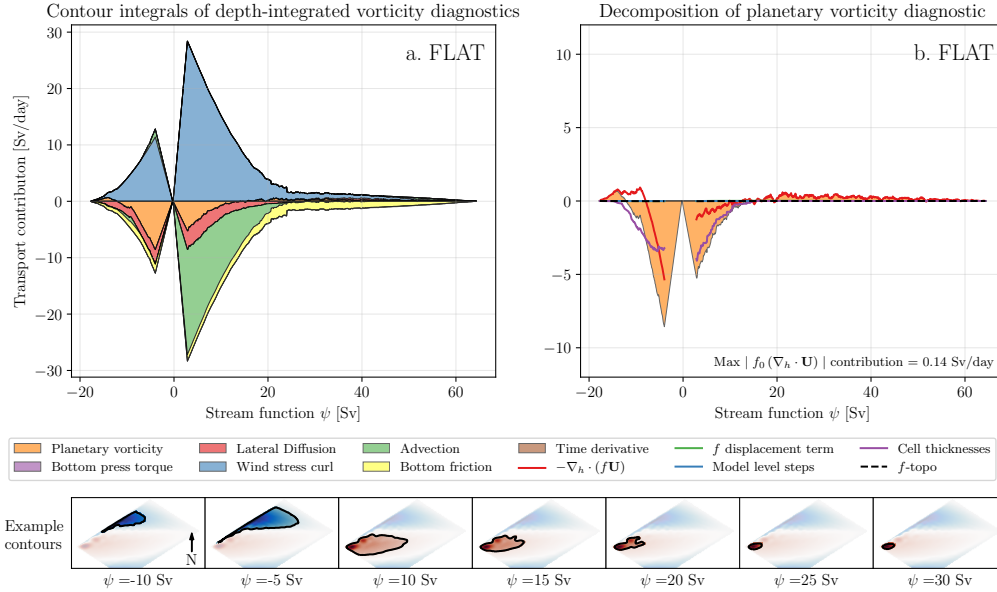


**Figure 9.** Stacked area plots showing the integrals of depth-integrated vorticity diagnostics (time-averaged) for the FLAT configuration. Positive values correspond to a force that spins the subtropical ( $\psi > 0$ ) or subpolar ( $\psi < 0$ ) gyre up. The diagnostics are integrated over areas enclosed by streamlines to develop a full forcing profile of the gyres. The  $x$  axis describes the value of the streamline used in the integration. Example streamline contours are given. (b) Shows the area integrals of the planetary vorticity diagnostic and its components. The maximum contour integral of  $|f_0(\nabla_h \cdot \mathbf{U})|$  is stated as an approximate error caused by the divergence of the depth-integrated flow.

511 In the SLOPED configuration (Figure 8) the advection and planetary vorticity di-  
 512 agnostics are still large but have an elongated structure similar to the SLOPED stream-  
 513 lines in Figure 5b. The bottom pressure torque is significant and is localized to the sloped  
 514 region (Figure 8b). The planetary vorticity diagnostic has a more complex decomposi-  
 515 tion as the influence of varying cell thicknesses extends beyond the edge of the domain  
 516 and model level steps also contribute (Figure 8k).

517 The integrals of the vorticity diagnostics over areas enclosed by streamlines are shown  
 518 in Figure 9 and Figure 10 for the FLAT and SLOPED configurations respectively as well  
 519 as the integrals of the planetary vorticity diagnostic components. The integrals are given  
 520 in units of Sv/day to describe the tendency for model forces to increase or decrease the  
 521 gyre transport over time. Example streamline contours are also shown. In these figures  
 522  $\psi > 0$  describes the subtropical gyre and  $\psi < 0$  describes the subpolar gyre. The sub-  
 523 tropical and subpolar gyres circulate in the opposite direction but the sign of the inte-  
 524 gration results are adjusted so that positive integrals correspond to forces that spin the  
 525 gyres up.

526 In the FLAT configuration we see that the subtropical and subpolar gyre are en-  
 527 tirely driven by wind stress curl. At the exterior of the subtropical gyre (small and pos-  
 528 itive values of  $\psi$ ) the wind stress curl is largely balanced by the advection of relative vor-  
 529 ticity which implies a net import of positive vorticity into the gyre. The imported vor-  
 530 ticity cannot originate from the subpolar gyre as the advection of relative vorticity plays  
 531 no role in spinning the subpolar gyre down. The streamlines at the exterior of the gyre

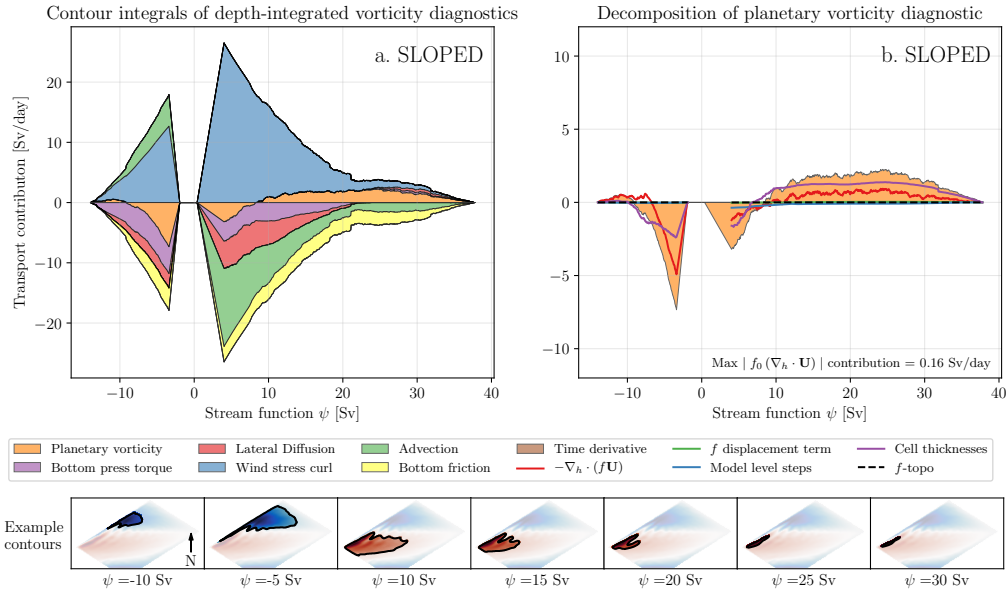


**Figure 10.** Stacked area plots showing the integrals of depth-integrated vorticity diagnostics (time-averaged) for the SLOPED configuration. Positive values correspond to a force that spins the subtropical ( $\psi > 0$ ) or subpolar ( $\psi < 0$ ) gyre up. (b) Shows the area integrals of the planetary vorticity diagnostic and its components.

532 envelop both cells (maxima in  $\psi$ ) of the subtropical gyre so the advection of vorticity  
 533 between the cells is not a contribution to the signal. The imported vorticity must origi-  
 534 nate from the recirculation gyre in the southernmost corner. In the subtropical gyre in-  
 535 terior the wind stress curl is largely balanced by the curl of bottom friction, matching  
 536 the balance proposed by Niiler (1966).

537 The planetary vorticity diagnostic is significant in both of the FLAT gyres and is  
 538 the dominant drag for the subpolar gyre. At both gyre exteriors (small values of  $\psi$ ) the  
 539 integrated planetary vorticity diagnostic is a combination of a numerical beta effect origi-  
 540 nating from the discrete calculation of  $-\nabla_h \cdot (f\mathbf{U})$  and the influence of partial  $F$  cells  
 541 that are artificially created by the EEN scheme. At the interior of both gyres (large val-  
 542 ues of  $\psi$ ) the numerical beta effect is the only component.

543 In the SLOPED configuration we see that both the subtropical and subpolar gyre  
 544 are almost entirely driven by wind stress curl. There is no dominant force spinning the  
 545 gyres down. Advection, bottom pressure torques, lateral diffusion, bottom friction, and  
 546 planetary vorticity all make a similar contribution to spinning the gyres down. The plan-  
 547 etary vorticity diagnostic is similarly mixed as both the numerical beta effect and par-  
 548 tial cells make up the signal. The gyres in the SLOPED configuration appear to be an  
 549 intermediate case between a topographically steered gyre and an advective regime.

550 Spurious forces that emerge from the discrete Coriolis acceleration are significant  
 551 in idealised models with and without variable bathymetry and appear to have a large  
 552 influence on gyre circulations. In the next sub-section we see if these forces are also sig-  
 553 nificant in a realistic global model.

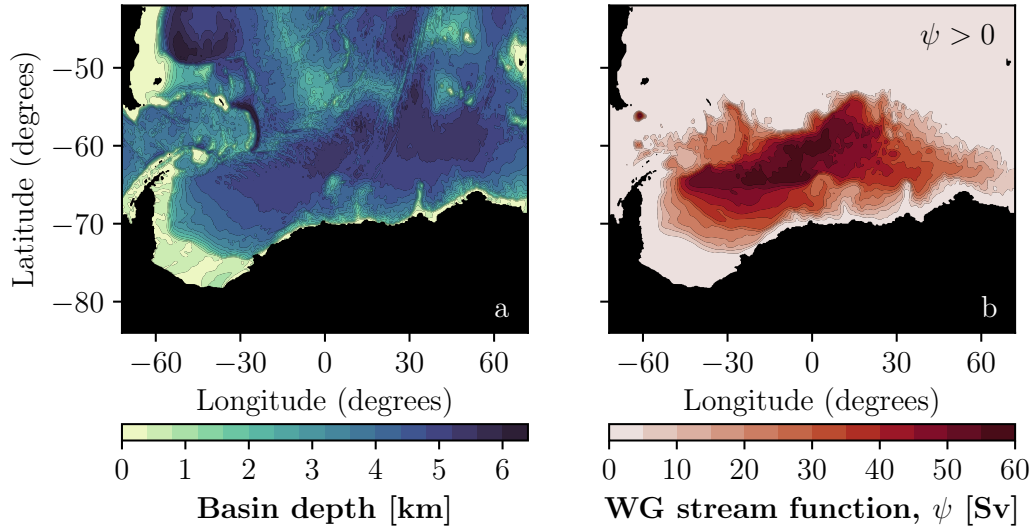


**Figure 11.** (a) The bathymetry of the Weddell Gyre region in the global model. (b) Depth-integrated streamfunction of the Weddell Gyre (time-averaged).

## 5 The Weddell Gyre

### 5.1 Details of the configuration

We now consider a more realistic configuration based on the NEMO global model with realistic forcing and bathymetry. In this experiment, we use an ocean-ice global configuration that is similar to that described in Storkey et al. (2018) but based on NEMO version 4. The global grid is based on the ‘ORCA’ family of grids within the NEMO framework (Madec et al., 2019). In this article we only consider the configuration using the ORCA025 grid ( $1/4^\circ$  horizontal resolution at the equator). Most of the model bathymetry for ORCA025 is derived from the ETOPO1 data set (Amante & Eakins, 2009). Bathymetry on the Antarctic shelf is based on IBSCO (Arndt et al., 2013) and has been smoothed by three applications of a first order Shapiro filter. The bathymetry is represented in  $z$ -coordinates by partial cells (Barnier et al., 2006). Surface forcing is taken from the CORE2 surface forcing data set (Large & Yeager, 2009) and includes contributions from sea ice. The bathymetry is shown in Figure 11a.

The model uses a free slip lateral boundary condition with a quadratic drag along the bottom boundaries and the TEOS-10 equation of state (McDougall & Barker, 2011). Biharmonic diffusion of momentum is implemented and acts along model level surfaces with a diffusivity that varies with local horizontal grid spacing (Willebrand et al., 2001). Laplacian diffusion of tracers is implemented and acts along isopycnal surfaces with a diffusivity that also varies with local horizontal grid spacing. The EEN vorticity scheme is used again for consistency with the analysis in Section 3 and the results in Section 4.

### 5.2 Methods

The methods used for calculating the depth-integrated streamfunction, vorticity diagnostics, and contour integrals are identical to those described in Section 4.2. We study the area including and surrounding the Weddell Gyre in the model (see Figure 11) and consider the time-averaged fields over a typical year. The stream function is interpolated onto a regular  $1/12^\circ$  grid and closed contours are identified for 201 values of  $\psi$ . Interpolating beyond  $1/12^\circ$  resolution makes little difference to the results, suggesting that

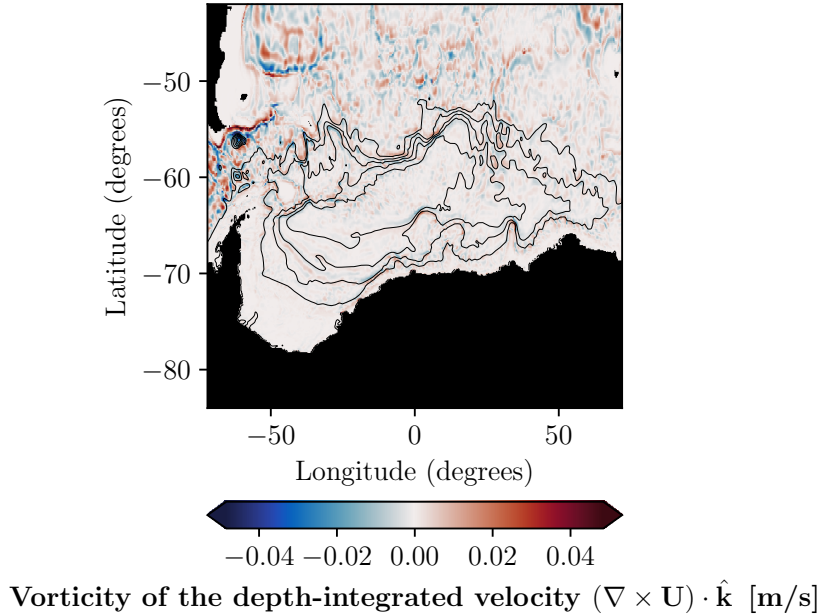


**Figure 12.** The vorticity of the depth-integrated velocity field (time-averaged) in the Weddell Gyre region of the global model. The black contours are positive streamlines ( $\psi > 0$ ) from Figure 11.

582 any area errors have been significantly suppressed. We test how closely the calculated  
 583 streamlines follow the circulation by integrating the positive quantity  $|f_0(\nabla_h \cdot \mathbf{U})|$   
 584 over the same enclosed areas to estimate the magnitude of the error caused by the divergent  
 585 flow. The maximum value of  $|f|$  is used as  $f_0$  and the largest contour integral of  $|f_0(\nabla_h \cdot \mathbf{U})|$   
 586 is 1.69 Sv/day which is substantially smaller than the leading contour integrals presented  
 587 in the next sub-section. In addition to this test we used an elliptical solver to decom-  
 588 pose the depth-integrated flow into a compressible and incompressible parts; using the  
 589 streamlines from the incompressible component does not change the results presented  
 590 in the next sub-section.

591 As we are studying a one gyre system we choose to only identify contours where  
 592  $\psi > 0$ . This effectively filters out the vorticity budget of closed circulations in the Antarc-  
 593 tic Circumpolar Current. The sign of the integration results are adjusted so that posi-  
 594 tive integrals correspond to forces that spin the Weddell Gyre up.

### 595 5.3 Results

596 The depth-integrated streamfunction of the Weddell Gyre is shown in Figure 11b  
 597 and it can be seen that the Weddell Gyre has a transport of 60 Sv. The streamlines fol-  
 598 low the isobaths closely suggesting the circulation is largely constrained by the bathymetry.  
 599 The vorticity of the depth-integrated velocity field is shown in Figure 12.

600 The depth-integrated vorticity diagnostics are shown in Figure 13. The fields shown  
 601 in Figure 13 have been smoothed using 25 point nearest neighbour averaging over a lo-  
 602 cal  $5 \times 5$  grid. The contribution from model level steps (Figure 13k) has not been smoothed  
 603 to show that it is localized to specific lines where the number of model levels change. The  
 604 combined effect of the wind stress and stress due to sea ice are shown in Figure 13e. With  
 605 realistic topography and forcing, the grid point values of depth-integrated vorticity di-  
 606 agnostics are very noisy (even when smoothed) with the exception of the surface stress

607 curl. This highlights how important it is to integrate the vorticity diagnostics when in-  
 608 terpreting them. For individual grid points we see that the planetary vorticity diagnos-  
 609 tic is made up of contributions from the beta effect, partial cells, and a significant con-  
 610 tribution from model level steps. The beta effect is the most coherent of the contribu-  
 611 tions and is mostly negative in the western limb of the gyre where  $V > 0$  and positive  
 612 in the eastern limb where  $V < 0$ . As expected, the contribution from model levels steps  
 613 is localized to areas where the number of model levels change.

614 Unlike in the double gyre model, bottom friction appears to be small and incoher-  
 615 ent in the Weddell Gyre region and is unlikely to have any significant influence on the  
 616 vorticity budget. The total time tendency (Figure 13d) is non-zero in this vorticity bud-  
 617 get suggesting that the model is not in a completely steady state; however, the grid point  
 618 values are only significant in the Drake Passage and are noisy.

619 The integrals of the depth-integrated vorticity diagnostics over areas enclosed by  
 620 streamlines are shown in Figure 14 alongside integrations of the planetary vorticity com-  
 621 ponents. We see that the Weddell Gyre is almost entirely spun up by the wind stress curl.  
 622 The stress due to sea ice (marked by hatching in Figure 14a) and the advection of rel-  
 623 ative vorticity also help to spin the Weddell Gyre up. The advective contribution is caused  
 624 by vorticity exchange at the interface between the Weddell Gyre and the ACC.

625 Bottom pressure torques and lateral diffusion play a notable role in spinning the  
 626 Weddell Gyre down but the planetary vorticity diagnostic is the most significant con-  
 627 tribution. Looking at the decomposition of the planetary vorticity diagnostic we see that  
 628 the signal is mostly determined by changes in model level and the remainder is deter-  
 629 mined by variations in cell thickness. This suggests that the Weddell Gyre is almost en-  
 630 tirely spun down by topography due to the combined effect of bottom pressure torques  
 631 and the planetary vorticity diagnostic, but the majority of the gyre’s interaction with  
 632 the sea floor is spurious. This conclusion is true in both the interior and exterior of the  
 633 gyre.

634 The results in Figure 14 are concerning as they suggest that the vorticity input from  
 635 the realistic surface stresses is largely balanced by spurious topographic accelerations.  
 636 In an area of the ocean with such strong bathymetric features, it is not surprising that  
 637 topographic forcing is important but we would expect the topographic accelerations from  
 638 a realistic bathymetry to also be realistic. Instead, the dominant component of the to-  
 639 pographic forcing is a spurious acceleration that is localized to discrete lines where the  
 640 number of model levels change (see Figure 13k) and arises from the masking of the non-  
 641 topographic Coriolis acceleration. This suggests that the partial cell representation of  
 642 the sea floor is not providing realistic topographic forcing in the Weddell Gyre region.

## 643 **6 Discussion**

644 We have shown that the vorticity dynamics of both highly idealized and realistic  
 645 gyre configurations are greatly influenced by spurious forces that emerge from the dis-  
 646 crete Coriolis force and the step-like representation of bathymetry. In the idealized dou-  
 647 ble gyre configuration (Section 4) the spurious force is a combination of numerical beta  
 648 and topographic effects that are present in both the FLAT and SLOPED configuration.  
 649 In the realistic Weddell Gyre (Section 5) the spurious force is the dominant drag and is  
 650 entirely determined by model level steps and partial cells. In this section we discuss pos-  
 651 sible methods to mitigate these spurious forces.

### 652 **6.1 Alternative vorticity schemes**

653 The results presented in Sections 4 and 5 both use the EEN vorticity scheme and  
 654 it is tempting to dismiss the spurious forces as an artifact of the selected scheme. The

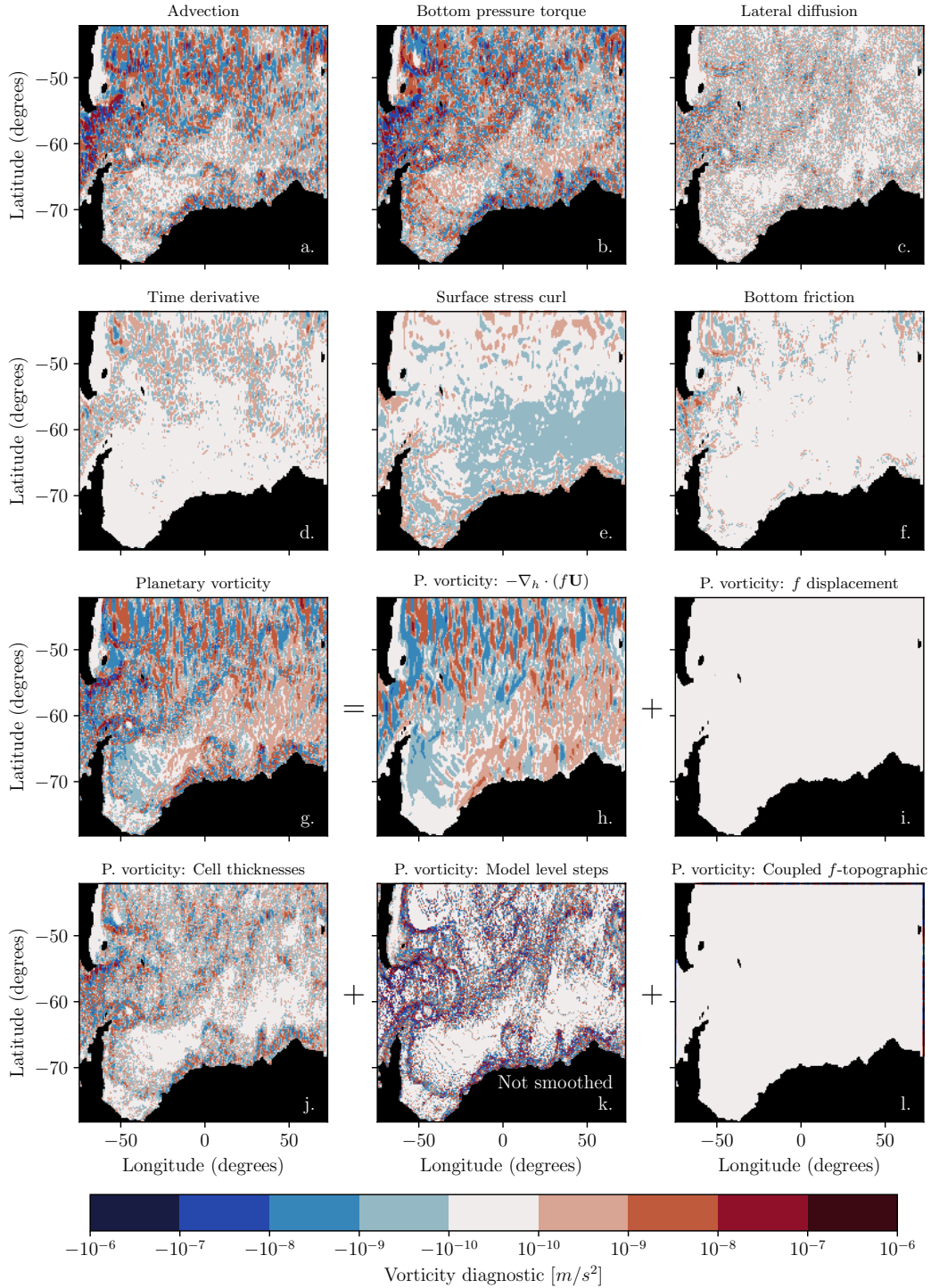


**Figure 13.** The depth-integrated vorticity diagnostics for the Weddell Gyre and the components of the planetary vorticity diagnostic (time-averaged). All fields except (k) have gone through a 25 point nearest neighbour smoothing process.

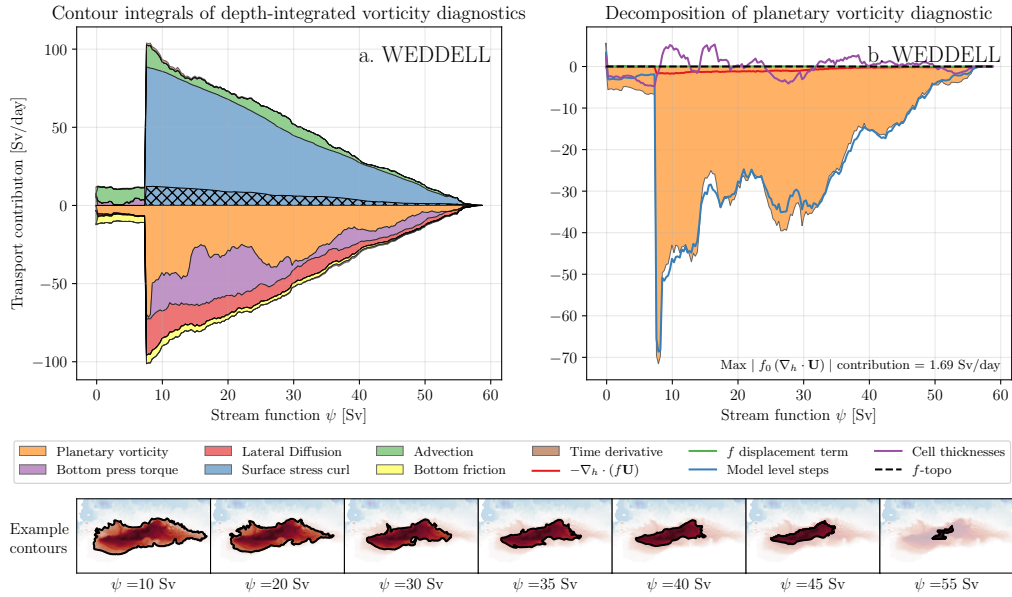


**Figure 14.** Stacked area plots showing the integrals of depth-integrated vorticity diagnostics for the Weddell Gyre (time-averaged). Positive values correspond to a force that spins the gyre up. The hatching marks the sea ice contribution to the surface stress integral. (b) Shows the area integrals of the planetary vorticity diagnostic and its components.

655 analysis in Section 3.2 is general for three popular schemes: EEN, ENE, and ENS. The  
 656 methods and decomposition used in this article are applicable under any scheme where  
 657 the Coriolis acceleration can be expressed in the form of Equations 8 and 9. Results from  
 658 the SLOPED double gyre configuration using the different schemes are presented in Ap-  
 659 pendix C and the vorticity budgets are qualitatively similar. Spurious topographic forces  
 660 and the numerical beta effect are still significant.

661 It therefore seems that switching between the available vorticity schemes will not  
 662 alleviate the spurious signal. It is possible that a new scheme could be formulated which  
 663 is designed to significantly reduce the spurious forces, but that will most likely require  
 664 abandoning the conserved quantities that characterise the existing schemes.

## 665 6.2 Alternative depth-integrated vorticity equations

666 In Section 2.1 we derived a depth-integrated vorticity equation by taking the curl  
 667 of the depth-integrated momentum equation and we calculated the model vorticity di-  
 668 agnostics using the equivalent discrete method. As discussed in Section 2.1, there are  
 669 alternative formulations of the depth-integrated vorticity equations with different phys-  
 670 ical meanings. An accurate model should be able to represent all forms of the depth-integrated  
 671 vorticity budget so switching between formulations does not alleviate any spurious forces,  
 672 but it is interesting to see if any of the spurious contributions in this article can spill over  
 673 into other vorticity budgets.

674 If we derive a continuous depth-integrated vorticity equation by depth-integrating  
 675 the curl of the momentum equations then the Coriolis acceleration emerges in the vor-

676 ticity budget as:

$$\int_{-H(x,y)}^{\eta(x,y,t)} \left[ \nabla \times \left( -f \hat{\mathbf{k}} \times \mathbf{u} \right)_h \right] \cdot \hat{\mathbf{k}} dz = -\nabla_h \cdot (f \mathbf{U}) + f (\mathbf{u}_b \cdot \nabla) H + f (\mathbf{u}_t \cdot \nabla) \eta, \quad (24)$$

677 where  $\mathbf{u}_t$  and  $\mathbf{u}_b$  are the horizontal velocities at the free surface and sea floor respectively.  
 678 When compared with Equation 2 we can see that the planetary vorticity term has an  
 679 additional topographic and free surface term. The second term on the right hand side  
 680 of Equation 24 describes a vortex stretching acting on the vertical velocity induced by  
 681 the bottom topography. In configurations with no variable bathymetry and small vari-  
 682 ations in the free surface, the order of taking the curl and depth-integrating no longer  
 683 affects the vorticity budget so the non-topographic spurious forces identified in this ar-  
 684 ticle will remain in either formulation.

685 To calculate the discrete curl of a horizontal vector field near the bathymetry we  
 686 need to make an assumption about how the along-slope component varies as it approaches  
 687 the edge of the domain. We can assume either a free slip or no slip boundary condition  
 688 by using a ghost point that mirrors the location of the closest grid point into the bathymetry.  
 689 For a free slip boundary condition the ghost point value matches the closest grid point  
 690 value,  $F^{\parallel}$ ; for a no slip boundary condition the ghost point value will be the negative  
 691 of the closest grid point value,  $-F^{\parallel}$ . A partial slip boundary condition also exists where  
 692 the value of the ghost point will be between  $-F^{\parallel}$  and  $F^{\parallel}$ .

693 Let us return to the simple flow introduced in Section 3.3 and illustrated in Fig-  
 694 ure 2 but this time when we calculate the planetary vorticity diagnostic we will calcu-  
 695 late the curl of the Coriolis acceleration on each model level and then depth-integrate.  
 696 For the lower level, the horizontal flow is entirely in the  $x$  direction so there is a zero along-  
 697 slope component of the Coriolis acceleration near the bathymetry ( $F^{\parallel}=0$ ). This means  
 698 that if a free slip, no-slip, or partial slip boundary condition are used the ghost point value  
 699 will be zero and the curl of the Coriolis force (centred on the purple cross in Figure 2)  
 700 will be zero in all three cases. As all vorticity generation takes place in the upper level,  
 701 the planetary vorticity diagnostic is the same if we take the curl before or after depth-  
 702 integrating (Equation 21) and the effect of model level steps can exist in either vortic-  
 703 ity budget.

704 The result of Equation 21 can be interpreted as a vortex stretching acting on the  
 705 vertical velocity  $U_1$ . The vertical velocity seems unlikely to originate from topographic  
 706 upwelling as there is no flow in the  $y$  direction. This fact combined with the ambiguity  
 707 of  $\nabla H$  at model level steps means we would advise caution before comparing the dis-  
 708 crete vortex stretching that originates from model level steps to the analytic vortex stretch-  
 709 ing in Equation 24.

### 710 6.3 The B-grid

711 Altering the grid geometry can significantly change the behaviour of model forces.  
 712 To highlight this we consider how the Coriolis force behaves on the B-grid. The B-grid  
 713 excels at representing geostrophic flows as  $u$ , and  $v$  are located on the same vector point.  
 714 The streamfunction and relative vorticity are located on the tracer point as shown in Fig-  
 715 ure 15.

716 On the B-grid the Coriolis acceleration is simply:

$$\text{COR}_{i,j,k}^x = f_{i,j} v_{i,j,k}, \quad (25)$$

$$\text{COR}_{i,j,k}^y = -f_{i,j} u_{i,j,k}. \quad (26)$$

717 The Coriolis acceleration does not rely on multi-point averaging or thickness weighting  
 718 of  $f$  so numerical contributions do not emerge in the grid point acceleration.

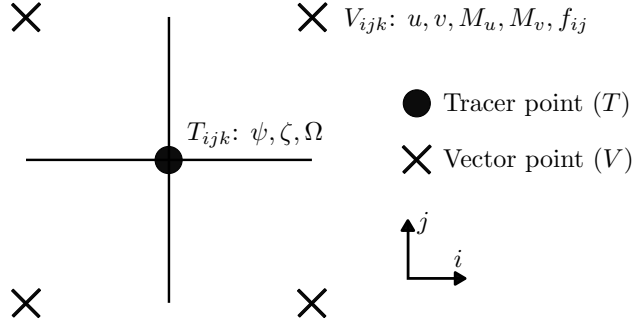


**Figure 15.** The horizontal distribution of variables on the B-grid. Tracer points (T) and vector points (V) are shown alongside important values that are centred on these points. Just like in the C-grid, the vertical velocities are found directly above and below the Tracer point.

719 On the B-grid  $u$  and  $v$  lie on the same point so they share the same mask. This  
 720 means that non-zero Coriolis accelerations are never masked near model level steps and  
 721 the depth-integrated Coriolis acceleration is a function of the depth-integrated veloci-  
 722 ties only:

$$\widehat{\text{COR}}_{i,j}^x = f_{i,j} V_{i,j}, \quad (27)$$

$$\widehat{\text{COR}}_{i,j}^y = -f_{i,j} U_{i,j}, \quad (28)$$

723 We therefore conclude that the spurious force caused by model level steps on the C-grid  
 724 (see Section 3.3) is not present on the B-grid. The corresponding planetary vorticity di-  
 725 agnostic is equal to  $-\nabla_h \cdot (f\mathbf{U})|_{i,j}$  calculated over a single tracer cell.

726 Calculating the curl on a B-grid is consistent with Stokes' law applied to a tracer  
 727 cell but the vector information is found on the corners of the cell. As the stream func-  
 728 tion is defined on the tracer point we can approximate that the area enclosed by a stream-  
 729 line is a collection of interior tracer cells. Similarly to the C-grid case in Section 3.5 this  
 730 is an approximation as we are assuming that the streamline follows the rectangular edges  
 731 of the interior tracer cells so interpolation may be required to remove any significant area  
 732 error. Unlike the C-grid case, the planetary vorticity diagnostic is equal to  $-\nabla_h \cdot (f\mathbf{U})|_{i,j}$   
 733 calculated over a single tracer cell. Therefore, the area integral of the planetary vortic-  
 734 ity diagnostic will satisfy the divergence theorem applied to the internal tracer cells. It  
 735 seems likely that this discrete integral may vanish on a sufficiently fine grid but further  
 736 investigation with idealized and realistic streamlines is needed.

737 Using the B-grid would remove all of the spurious topographic forces identified in  
 738 this article. This highlights how a model circulation's interaction with the sea floor is  
 739 significantly affected by the grid geometry.

#### 740 6.4 Terrain-following coordinates

741 The spurious topographic effects found in this article are a consequence of how bot-  
 742 tom topography is represented in  $z$ -coordinates. In the Weddell Gyre especially we see  
 743 how model level steps can create large spurious contributions to the depth-integrated vor-  
 744 ticity budget.

745 Terrain-following coordinates (or  $\sigma$ -coordinates) are an alternative form of verti-  
 746 cal coordinate where the vertical resolution adjusts with the bottom topography so that  
 747 the same number of model levels are present in all fluid columns (Song & Haidvogel, 1994).  
 748  $\sigma$ -coordinates are used in Stewart et al. (2021), Schoonover et al. (2016), and Jackson

et al. (2006) and have the advantage of removing spurious terms that emerge from model level steps. The forms of the EEN, ENE, and ENS vorticity schemes are unchanged when using terrain-following coordinates so the horizontal variations in cell thicknesses could still cause a spurious signal.

Terrain-following coordinates are not used widely in climate models because of the difficulty in calculating accurate horizontal pressure gradients (near the equator), advection, and isoneutral tracer advection. A full discussion of the current advantages and limitations of terrain following coordinates can be found in Lemarié et al. (2012).

## 6.5 Isopycnal coordinates and the vertical Lagrangian-remap method

In isopycnal C-grid models, where density is used as a vertical coordinate, cell thicknesses still vary and in models with many density layers the model levels are free to incrop to the sea floor. The forms of the EEN, ENS, and ENE schemes are unchanged when using density coordinates so the spurious signals in the planetary vorticity diagnostic seem to be possible. In configurations where density layers infrequently incrop to the sea floor, the effect of model level steps will be significantly suppressed as the grid is approaching the limit of a terrain-following coordinate system.

In C-grid models that use the vertical Lagrangian-remap method (Bleck, 2002; Adcroft et al., 2019) the vertical coordinate evolves with the flow and is then conservatively remapped onto a target grid (see Griffies et al. (2020) for a review). The forms of the EEN, ENS, and ENE schemes are unchanged when using this method. If the target coordinate grid still has horizontal variations in cell thicknesses and incrops with the sea floor, we would expect there to be spurious topographic interactions with the sea floor. It is possible that in areas of topographic upwelling the effect of model level steps could be reduced as Coriolis accelerations near the bathymetry are elevated by the vertical motion and are partially projected onto unmasked points when remapped onto the target grid.

## 7 Summary

The depth-integrated vorticity budget is a valuable tool for identifying important model forces in gyre circulations. Vorticity diagnostics can be integrated over the area enclosed by streamlines to identify forces responsible for spinning the gyre up and down. By considering how the vorticity budget is represented on a C-grid with step-like bathymetry we identified spurious forces that emerge from the representation of bottom topography and the discrete Coriolis acceleration. Model level steps and partial cells produce two distinct spurious topographic forces. In the absence of bottom topography, it is shown that the discrete planetary vorticity term does not generally vanish when integrated over the discrete area enclosed by a streamline. This suggests that a spurious non-topographic force, described as a numerical beta effect, is also present.

We first studied the vorticity budget of an idealized double gyre configuration with analytic geometry, forcing, and two bathymetry options. The FLAT variant has a constant depth and the SLOPED variant has a linear slope that extends over half the domain. The subtropical gyre of the FLAT configuration is non-linear at the exterior (wind stress curl balanced by advection) and is in a Stommel (1948) regime in the interior (wind stress curl balanced by friction). The FLAT subpolar gyre is spun up by wind stress curl and mostly spun down by spurious forces found in the planetary vorticity diagnostic. Spurious forces are significant in both FLAT gyres and are a consequence of the numerical beta effect and partial  $F$  cells that are artificially introduced by the EEN vorticity scheme. Artificial partial  $F$  cells would not be present in the ENS or ENE vorticity schemes.

796 The vorticity budget of the SLOPED gyres features bottom pressure torques and  
 797 an increased influence of partial cells on the planetary vorticity diagnostic. The SLOPED  
 798 subtropical gyre is an intermediate case between a topographically steered gyre and a  
 799 non-linear circulation. The SLOPED subpolar gyre is driven by wind stress curl but spun  
 800 down by the combined effect of bottom pressure torques and spurious interactions with  
 801 the topography via partial cells. This first case study highlighted how spurious terms  
 802 can dominate a vorticity budget in idealized configurations with and without variable  
 803 bathymetry.

804 The second case study was the Weddell Gyre in a global model where the forcing  
 805 and geometry are more realistic. By studying the vorticity budget of the Weddell Gyre  
 806 we conclude that the model circulation is mostly spun up by wind stress curl and spun  
 807 down by the combined effect of bottom pressure torques and spurious interactions with  
 808 the topography. The largest of the topographic forces spinning the Weddell Gyre down  
 809 is the spurious and unrealistic force caused by model level steps.

810 Switching to alternative vorticity schemes is not effective at reducing spurious con-  
 811 tributions to the vorticity budget. By presenting a general form of the discrete Corio-  
 812 lis acceleration we are able to quickly conclude that the topographic and non-topographic  
 813 spurious forces will remain under all three vorticity schemes and any other scheme that  
 814 uses this general form. The influence of model level steps is a direct consequence of the  
 815 C-grid geometry when using vertical coordinates that intersect the bathymetry and is  
 816 relatively insensitive to the choice of vorticity scheme.

817 Altering the geometry of the discretisation is an effective method for reducing spu-  
 818 rious topographic forces. The B-grid is better at representing the Coriolis force and it  
 819 is not possible for model level steps or partial cells to influence the Coriolis acceleration.  
 820 Model level steps and their influence on the Coriolis acceleration can be avoided alto-  
 821 gether by using terrain-following coordinates.

822 The B-grid and terrain-following coordinates have their own unique limitations and  
 823 it is unclear how much the identified spurious forces corrupt circulation variables such  
 824 as the gyre transport. It is possible that the spurious forces are inadvertently perform-  
 825 ing the role of one or more real ocean processes that are required for accurate simula-  
 826 tions. If a combination of non-spurious forces can fully account for the spurious forces  
 827 found in this article then the identified problem is purely diagnostic in nature. Other-  
 828 wise, any part of the spurious forcing that cannot be accounted for by non-spurious forces  
 829 should be considered as a numerical error. This numerical error could be small but may  
 830 also accumulate under specific conditions and corrupt model circulations. The spurious  
 831 cooling (Hecht, 2010) that occurs when a dispersive advection scheme is used with the  
 832 Gent and McWilliams (1990) eddy parametrization highlights the dangers of ignoring  
 833 numerical errors.

834 It is also possible that other model forces contain spurious contributions that have  
 835 not been uncovered in this article. These contributions could be significant and may have  
 836 the potential to cancel the spurious effects found in this article. When looking at the in-  
 837 tegrated diagnostics in Figures 9, 10, and 14 we see that usually the only model force  
 838 with an opposite contribution to the Coriolis force that is large enough to cancel the found  
 839 spurious effects is the surface stress. It seems unlikely that the surface stress contains  
 840 spurious contributions that are closely tied to bathymetry and the Coriolis parameter.

841 It is important for the ocean modelling community to continue developing new ways  
 842 of representing bathymetry and we hope that vorticity budgets and the diagnostic method  
 843 presented in this article will provide a valuable tool for assessing and quantifying rep-  
 844 resentations of the sea floor in current and future ocean models.

## Appendix A Deriving the depth-integrated vorticity equation

Here we derive the depth-integrated vorticity equation (Equation 2) including the omitted contributions from surface undulations and atmospheric pressure torques. We start from the vector invariant form of the momentum equation,

$$\frac{\partial \mathbf{u}_h}{\partial t} = - \left[ (\nabla \times \mathbf{u}) \times \mathbf{u} + \frac{1}{2} \nabla (\mathbf{u} \cdot \mathbf{u}) \right]_h - f \left( \hat{\mathbf{k}} \times \mathbf{u} \right)_h - \frac{1}{\rho_0} \nabla_h P + \mathcal{F}^{\mathbf{u}} + \mathcal{D}^{\mathbf{u}}, \quad (\text{A1})$$

which has already been introduced in Section 2.1. To derive the depth-integrated vorticity equation, we must first depth-integrate the equation and then calculate the vertical component of the curl. In this appendix, we consider how each term in Equation A1 is transformed by this operation.

When depth-integrating the time derivative term in Equation A1, we must respect the time dependency of the free surface,  $\eta$ . We therefore use the Leibniz integration rule,

$$\nabla \times \left( \int_{-H(x,y)}^{\eta(x,y,t)} \frac{\partial \mathbf{u}_h}{\partial t} dz \right) \cdot \hat{\mathbf{k}} = \frac{\partial}{\partial t} (\nabla \times \mathbf{U}) \cdot \hat{\mathbf{k}} - \nabla \times \left( \mathbf{u}_h(z = \eta) \frac{\partial \eta}{\partial t} \right) \cdot \hat{\mathbf{k}}, \quad (\text{A2})$$

where the second term on the right hand side of Equation A2 is the contribution from free surface undulations.

The non-linear term in Equation A1 can be rewritten as,

$$\left[ (\nabla \times \mathbf{u}) \times \mathbf{u} + \frac{1}{2} \nabla (\mathbf{u} \cdot \mathbf{u}) \right]_h = \frac{1}{2} \nabla_h (\mathbf{u}_h \cdot \mathbf{u}_h) + \zeta \left( \hat{\mathbf{k}} \times \mathbf{u} \right)_h + w \frac{\partial \mathbf{u}_h}{\partial z}. \quad (\text{A3})$$

The non-linear term emerges as the advection term in the depth-integrated vorticity equation and we note that,

$$\nabla \times \left[ \int_{-H}^{\eta} \zeta \left( \hat{\mathbf{k}} \times \mathbf{u} \right)_h dz \right] \cdot \hat{\mathbf{k}} = \nabla_h \cdot \left( \int_{-H}^{\eta} \zeta \mathbf{u}_h dz \right). \quad (\text{A4})$$

Similarly the curl of the depth-integrated Coriolis acceleration is the planetary vorticity term,

$$\nabla \times \left[ \int_{-H}^{\eta} -f \left( \hat{\mathbf{k}} \times \mathbf{u} \right)_h dz \right] \cdot \hat{\mathbf{k}} = -\nabla_h \cdot (f \mathbf{U}). \quad (\text{A5})$$

When depth-integrating the pressure gradient in Equation A1, we must respect the  $x$  and  $y$  dependency of the sea floor and the free surface. We therefore use the Leibniz integration rule,

$$\nabla \times \left( \int_{-H(x,y)}^{\eta(x,y,t)} -\frac{1}{\rho_0} \nabla_h P dz \right) \cdot \hat{\mathbf{k}} = \frac{1}{\rho_0} (\nabla P_b \times \nabla H) \cdot \hat{\mathbf{k}} + \frac{1}{\rho_0} (\nabla P_a \times \nabla \eta) \cdot \hat{\mathbf{k}}, \quad (\text{A6})$$

where  $P_a$  is the atmospheric pressure at the free surface. The second term on the right hand side of Equation A6 is the atmospheric pressure torque.

The surface forcing term in Equation A1 emerges as the difference between the curl of the top and bottom stresses,

$$\nabla \times \left( \int_{-H}^{\eta} \mathcal{F}^{\mathbf{u}} dz \right) \cdot \hat{\mathbf{k}} = \frac{1}{\rho_0} (\nabla \times \boldsymbol{\tau}_{\text{top}}) \cdot \hat{\mathbf{k}} - \frac{1}{\rho_0} (\nabla \times \boldsymbol{\tau}_{\text{bot}}) \cdot \hat{\mathbf{k}}, \quad (\text{A7})$$

$$(\text{A8})$$

and the diffusion term emerges as  $\mathcal{D}^\zeta$ ,

$$\nabla \times \left( \int_{-H}^{\eta} \mathcal{D}^{\mathbf{u}} dz \right) \cdot \hat{\mathbf{k}} = \mathcal{D}^\zeta. \quad (\text{A9})$$

By combining all the equations above we can derive the depth-integrated vorticity equation,

$$\begin{aligned}
 \frac{\partial}{\partial t} (\nabla \times \mathbf{U}) \cdot \hat{\mathbf{k}} = & - \nabla_h \cdot (f\mathbf{U}) + \frac{1}{\rho_0} (\nabla P_b \times \nabla H) \cdot \hat{\mathbf{k}} + \frac{1}{\rho_0} (\nabla \times \boldsymbol{\tau}_{\text{top}}) \cdot \hat{\mathbf{k}} \\
 & - \frac{1}{\rho_0} (\nabla \times \boldsymbol{\tau}_{\text{bot}}) \cdot \hat{\mathbf{k}} + \mathcal{D}^\zeta \\
 & - \nabla_h \cdot \left( \int_{-H(x,y)}^{\eta(x,y,t)} \zeta \mathbf{u} dz \right) - \left[ \nabla \times \left( \int_{-H(x,y)}^{\eta(x,y,t)} \frac{1}{2} \nabla_h (\mathbf{u}_h^2) + w \frac{\partial \mathbf{u}_h}{\partial z} \right) \right] \cdot \hat{\mathbf{k}} \\
 & + \underbrace{\frac{1}{\rho_0} (\nabla P_a \times \nabla \eta) \cdot \hat{\mathbf{k}}}_{\text{Atmospheric pressure torque}} + \underbrace{\left[ \nabla \times \left( \mathbf{u}_h(z = \eta) \frac{\partial \eta}{\partial t} \right) \right] \cdot \hat{\mathbf{k}}}_{\text{Surface undulations}}. \quad (\text{A10})
 \end{aligned}$$

## Appendix B Explicit forms of the Coriolis schemes

Here we explicitly state the forms of the discrete Coriolis acceleration in the ENE, ENS, and EEN vorticity schemes for a  $z$ -coordinate system. In the ENE vorticity scheme the  $x$  and  $y$  components of the Coriolis acceleration are:

$$\begin{aligned}
 \text{COR}_{i,j,k}^x &= \frac{1}{4e_{i,j}^{1u}} \left[ f_{i,j-1} \left( (ve^{1v})_{i,j-1,k} + (ve^{1v})_{i+1,j-1,k} \right) \right. \\
 &\quad \left. + f_{i,j} \left( (ve^{1v})_{i,j,k} + (ve^{1v})_{i+1,j,k} \right) \right], \\
 \text{COR}_{i,j,k}^y &= \frac{1}{4e_{i,j}^{2v}} \left[ f_{i-1,j} \left( (ue^{2u})_{i-1,j,k} + (ue^{2u})_{i-1,j+1,k} \right) \right. \\
 &\quad \left. + f_{i,j} \left( (ue^{2u})_{i,j,k} + (ue^{2u})_{i,j+1,k} \right) \right]. \quad (\text{B1})
 \end{aligned}$$

In the ENS vorticity scheme the  $x$  and  $y$  components of the Coriolis acceleration are:

$$\begin{aligned}
 \text{COR}_{i,j,k}^x &= \frac{1}{8e_{i,j}^{1u}} \left[ (ve^{1v})_{i,j-1,k} + (ve^{1v})_{i+1,j-1,k} \right. \\
 &\quad \left. + (ve^{1v})_{i,j,k} + (ve^{1v})_{i+1,j,k} \right] [f_{i,j-1} + f_{i,j}], \\
 \text{COR}_{i,j,k}^y &= \frac{-1}{8e_{i,j}^{2v}} \left[ (ue^{2u})_{i-1,j-1,k} + (ue^{2u})_{i-1,j+1,k} \right. \\
 &\quad \left. + (ue^{2u})_{i,j,k} + (ue^{2u})_{i,j+1,k} \right] [f_{i-1,j} + f_{i,j}]. \quad (\text{B2})
 \end{aligned}$$

We note that each term in the ENE and ENS forms can be written in the general form of Equations 8 and 9 as  $ve^{1v} = \tilde{V}/e^{3v}$  and  $ue^{2u} = \tilde{U}/e^{3u}$ . In the ENE and ENS cases  $e_k^3(\mathbf{b}_n) = e_k^3(\mathbf{c}_n)$  in Equations 8 and 9.

In the EEN vorticity scheme, the  $x$  and  $y$  components of the Coriolis acceleration are:

$$\begin{aligned}
 \text{COR}_{i,j,k}^x &= \frac{1}{12e_{i,j}^{1u}} \left[ F_{i,j,k}^{NE} (ve^{3v} e^{1v})_{i,j,k} + F_{i+1,j,k}^{NW} (ve^{3v} e^{1v})_{i+1,j,k} \right. \\
 &\quad \left. + F_{i,j,k}^{SE} (ve^{3v} e^{1v})_{i,j-1,k} + F_{i+1,j,k}^{SW} (ve^{3v} e^{1v})_{i+1,j-1,k} \right], \\
 \text{COR}_{i,j,k}^y &= \frac{-1}{12e_{i,j}^{2v}} \left[ F_{i,j,k}^{NE} (ue^{3u} e^{2u})_{i,j,k} + F_{i,j,k}^{NW} (ue^{3u} e^{2u})_{i-1,j,k} \right. \\
 &\quad \left. + F_{i,j+1,k}^{SE} (ue^{3u} e^{2u})_{i,j+1,k} + F_{i,j+1,k}^{SW} (ue^{3u} e^{2u})_{i-1,j+1,k} \right], \quad (\text{B3})
 \end{aligned}$$

896 where  $F^{NE}$ ,  $F^{NW}$ ,  $F^{SE}$ , and  $F^{SW}$  are thickness-weighted triads of the Coriolis param-  
 897 eter:

$$F_{i,j,k}^{NE} = \left( \tilde{f}_{i,j,k} + \tilde{f}_{i-1,j,k} + \tilde{f}_{i,j-1,k} \right), \quad (\text{B4})$$

$$F_{i,j,k}^{NW} = \left( \tilde{f}_{i,j,k} + \tilde{f}_{i-1,j,k} + \tilde{f}_{i-1,j-1,k} \right), \quad (\text{B5})$$

$$F_{i,j,k}^{SE} = \left( \tilde{f}_{i,j,k} + \tilde{f}_{i,j-1,k} + \tilde{f}_{i-1,j-1,k} \right), \quad (\text{B6})$$

$$F_{i,j,k}^{SW} = \left( \tilde{f}_{i-1,j,k} + \tilde{f}_{i,j-1,k} + \tilde{f}_{i-1,j-1,k} \right), \quad (\text{B7})$$

898 where  $\tilde{f} = f/e^{3f}$  using the EEN definition of  $e^{3f}$  shown in Equation 13.

899 To calculate the planetary vorticity diagnostic we take the curl of the depth-integrated  
 900 Coriolis acceleration using Equations 15 and 22. In general the resulting equation of the  
 901 vorticity diagnostic is very difficult to interpret. We only present the form of the plan-  
 902 etary vorticity diagnostic for the EEN scheme on a grid with no partial cells or model  
 903 level steps as it is used to derive the numerical beta effect in Section 3.5:

$$\begin{aligned} \text{PVO}_{i,j} = & \frac{1}{12(e^{1f}e^{2f})_{i,j}} \left[ -f_{i,j+1}^{NE} (Ve^{1v})_{i,j+1} - f_{i+1,j+1}^{NW} (Ve^{1v})_{i+1,j+1} \right. \\ & + f_{i,j}^{SE} (Ve^{1v})_{i,j-1} + f_{i+1,j}^{SW} (Ve^{1v})_{i+1,j-1} \\ & - f_{i+1,j+1}^{SE} (Ue^{2u})_{i+1,j+1} - f_{i+1,j}^{NE} (Ue^{2u})_{i+1,j} \\ & + f_{i,j+1}^{SW} (Ue^{2u})_{i-1,j+1} + f_{i,j}^{NW} (Ue^{2u})_{i-1,j} \\ & - (f_{i,j+1} - f_{i,j-1}) \left( (Ve^{1v})_{i+1,j} + (Ve^{1v})_{i,j} \right) \\ & \left. - (f_{i+1,j} - f_{i-1,j}) \left( (Ue^{2u})_{i,j+1} + (Ue^{2u})_{i,j} \right) \right]. \quad (\text{B8}) \end{aligned}$$

## 904 **Appendix C Alternative vorticity schemes in the double gyre model**

905 In this section we present various integrations of the SLOPED double gyre config-  
 906 uration using different vorticity schemes: EEN, ENS, and ENE. All other aspects of the  
 907 experiment are as described in Section 4.1. The results are shown in Figure C1. The vor-  
 908 ticity budget is qualitatively similar between the three cases as well as the decomposi-  
 909 tion of the planetary vorticity diagnostic. It should be noted that the circulations do dif-  
 910 fer as the transports vary and the separation points of the western boundary currents  
 911 change.

## 912 **Appendix D Contour integration without interpolation**

913 The interpolation of vorticity diagnostic fields and the streamfunction is discussed  
 914 in Section 4.2. Linear interpolation is used to minimise the difference between the en-  
 915 closed area of the true streamline and the total area of the interior  $F$  cells. In this sec-  
 916 tion we present results that use uninterpolated fields from the FLAT double gyre con-  
 917 figuration. The results are shown in Figure D1 and are qualitatively similar to the in-  
 918 terpolated results shown in Figure 9. This example is selected to demonstrate both the  
 919 qualitative similarity to interpolated results but also the reduced coherence that comes  
 920 from using non-interpolated data. The non-interpolated results from the Weddell Gyre  
 921 are in fact more coherent than the results shown in Figure D1.

## 922 **Acknowledgments**

923 This work was financially supported by the Natural Environment Research Council NE/S007474/1.  
 924 This work used Monsoon2, a collaborative High-Performance Computing facility funded  
 925 by the Met Office and the Natural Environment Research Council and used JASMIN,

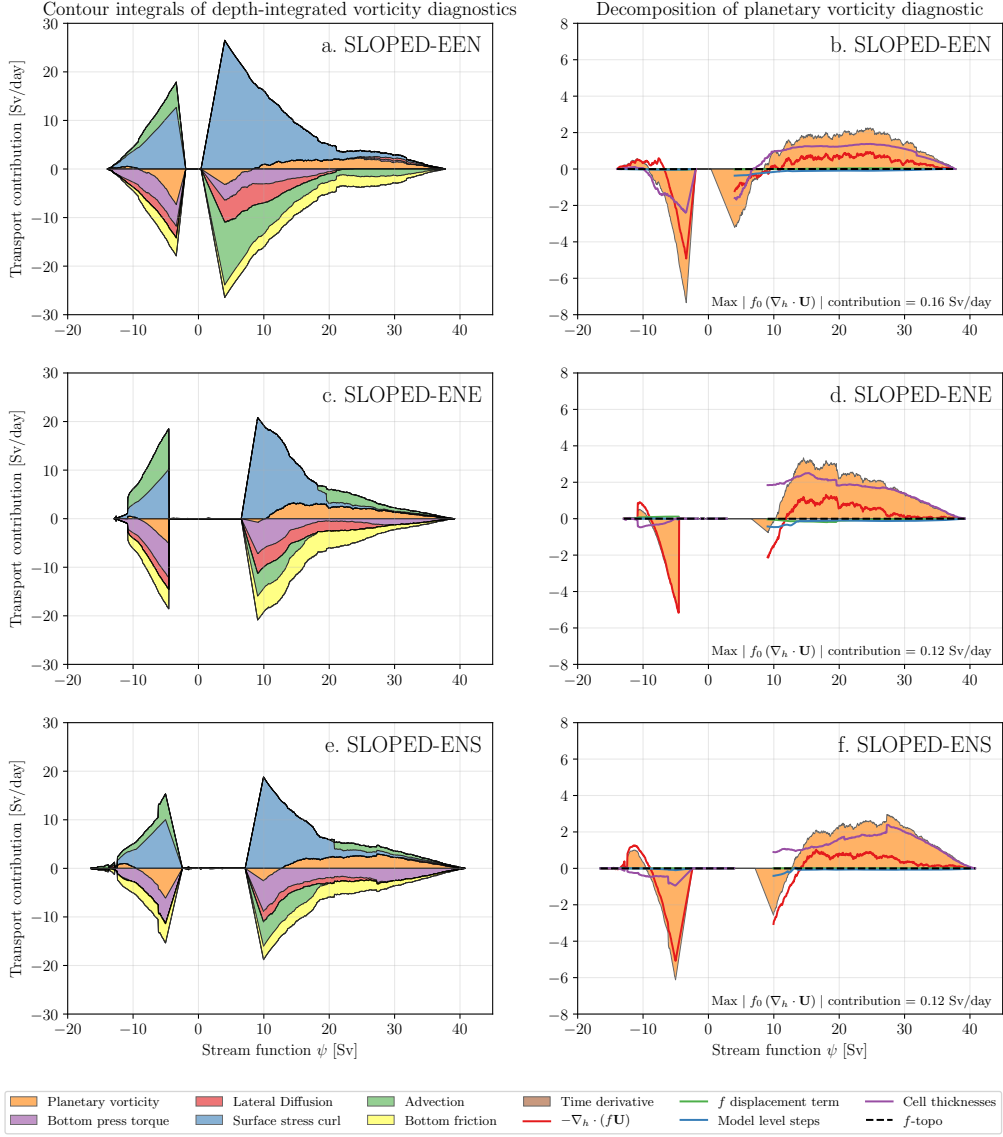


**Figure C1.** Stacked area plots showing the integrals of depth-integrated vorticity diagnostics for the SLOPED configuration (time-averaged) using the EEN, ENE, and ENS vorticity schemes. Positive values correspond to a force that spins the subtropical ( $\psi > 0$ ) or subpolar ( $\psi < 0$ ) gyre up. A decomposition of the planetary vorticity diagnostic integrals are given on the right (b,d,f).

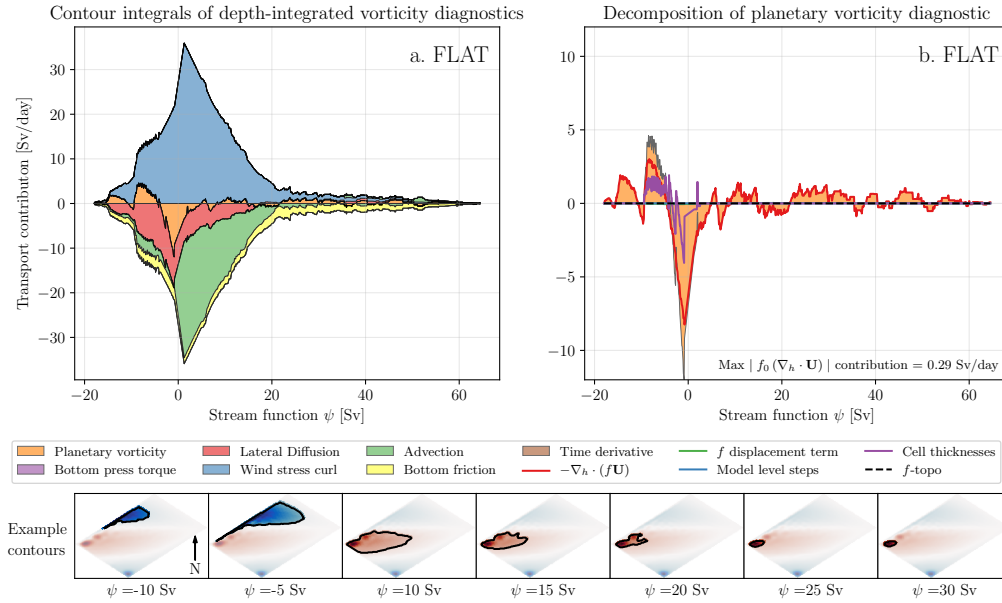


**Figure D1.** Stacked area plots showing the integrals of depth-integrated vorticity diagnostics (time-averaged) for the FLAT configuration without using interpolated fields. Positive values correspond to a force that spins the subtropical ( $\psi > 0$ ) or subpolar ( $\psi < 0$ ) gyre up. (b) Shows the area integrals of the planetary vorticity diagnostic and its components. The vorticity budget and decomposition are qualitatively similar to that shown in Figure 9.

926 the UK collaborative data analysis facility. We would like to thank Julian Mak and An-  
 927 drew Coward for their assistance in configuring NEMO on Monsoon2. We would also like  
 928 to thank Stephen Griffies, Hemant Khatri, and two anonymous reviewers for their de-  
 929 tailed comments that improved the manuscript.

930 The software used to calculate, integrate, and plot the vorticity budget is available  
 931 from <https://github.com/afstyles/VorticityContourAnalysisForNemo/tree/917f337/>. The  
 932 model integrations can be found on Zenodo (Styles et al., 2022).

933 The global configuration used in this article uses NEMO version 4.0.4 with the fol-  
 934 lowing merged branches:

- 935 • branches/UKMO/NEMO\_4.0.4\_mirror @ 14075,
- 936 • branches/UKMO/NEMO\_4.0.4\_GO8\_package @ 14474,
- 937 • branches/UKMO/NEMO\_4.0.4\_GO6\_mixing @ 14099,
- 938 • branches/UKMO/NEMO\_4.0.4\_old\_tidal\_mixing @ 14096,
- 939 • branches/UKMO/NEMO\_4.0.4\_momentum\_trends @ 15194.

940 The double gyre configuration uses NEMO version 4.0.1 and any modified source code  
 941 is archived on Zenodo (Styles et al., 2022). The versions of NEMO and the mentioned  
 942 branches can be found at <https://forge.ipsl.jussieu.fr/nemo/browser/NEMO/>.

## 943 References

944 Adcroft, A., Anderson, W., Balaji, V., Blanton, C., Bushuk, M., Dufour, C. O., ...  
 945 Zhang, R. (2019). The GFDL Global Ocean and Sea Ice Model OM4.0: Model

- 946 Description and Simulation Features. *Journal of Advances in Modeling Earth*  
 947 *Systems*, 11(10), 3167–3211. doi: 10.1029/2019MS001726
- 948 Amante, C., & Eakins, B. W. (2009). ETOPO1 arc-minute global relief model: pro-  
 949 cedures, data sources and analysis. *NOAA Technical Memorandum NESDIS*  
 950 *NGDC-24*.
- 951 Arakawa, A., & Lamb, V. R. (1981). A potential enstrophy and energy conserving  
 952 scheme for the shallow water equations. *Monthly Weather Review*, 109(1), 18–  
 953 36.
- 954 Arndt, J. E., Schenke, H. W., Jakobsson, M., Nitsche, F. O., Buys, G., Goleby,  
 955 B., ... Wigley, R. (2013, jun). The International Bathymetric Chart of the  
 956 Southern Ocean (IBCSO) Version 1.0-A new bathymetric compilation covering  
 957 circum-Antarctic waters. *Geophysical Research Letters*, 40(12), 3111–3117.  
 958 doi: 10.1002/grl.50413
- 959 Barnier, B., Madec, G., Penduff, T., Molines, J. M., Treguier, A. M., Le Sommer, J.,  
 960 ... De Cuevas, B. (2006). Impact of partial steps and momentum advection  
 961 schemes in a global ocean circulation model at eddy-permitting resolution.  
 962 *Ocean Dynamics*, 56(5-6), 543–567. doi: 10.1007/s10236-006-0082-1
- 963 Bell, M. J. (1999). Vortex stretching and bottom torques in the Bryan-Cox ocean  
 964 circulation model. *Journal of Geophysical Research: Oceans*. doi: 10.1029/  
 965 1999jc900064
- 966 Bleck, R. (2002, jan). An oceanic general circulation model framed in hy-  
 967 brid isopycnic-Cartesian coordinates. *Ocean Modelling*, 4(1), 55–88. doi:  
 968 10.1016/S1463-5003(01)00012-9
- 969 Cane, M. A., Kamenkovich, V. M., & Krupitsky, A. (1998). On the utility and  
 970 disutility of JEBAR. *Journal of Physical Oceanography*. doi: 10.1175/1520  
 971 -0485(1998)028<0519:OTUADO>2.0.CO;2
- 972 Drijfhout, S. S., Marshall, D. P., & Dijkstra, H. A. (2013). Conceptual Models of  
 973 the Wind-Driven and Thermohaline Circulation. In G. Siedler, S. M. Griffies,  
 974 J. Gould, & J. A. Church (Eds.), *Ocean circulation and climate* (Vol. 103, pp.  
 975 257–282). Academic Press. doi: 10.1016/B978-0-12-391851-2.00011-8
- 976 Gent, P. R., & McWilliams, J. C. (1990). Isopycnal Mixing in Ocean Circulation  
 977 Models. *Journal of Physical Oceanography*. doi: 10.1175/1520-0485(1990)  
 978 020<0150:imiocm>2.0.co;2
- 979 Griffies, S. M., Adcroft, A., & Hallberg, R. W. (2020). A Primer on the Vertical  
 980 Lagrangian-Remap Method in Ocean Models Based on Finite Volume Gener-  
 981 alized Vertical Coordinates. *Journal of Advances in Modeling Earth Systems*,  
 982 12(10), 1–38. doi: 10.1029/2019MS001954
- 983 Gula, J., Molemaker, M. J., & McWilliams, J. C. (2015). Gulf stream dynamics  
 984 along the southeastern U.S. seaboard. *Journal of Physical Oceanography*,  
 985 45(3), 690–715. doi: 10.1175/JPO-D-14-0154.1
- 986 Hecht, M. W. (2010). Cautionary tales of persistent accumulation of numerical error:  
 987 Dispersive centered advection. *Ocean Modelling*, 35(3), 270–276. doi: 10.1016/  
 988 j.ocemod.2010.07.005
- 989 Hughes, C. W., & de Cuevas, B. A. (2001). Why western boundary currents in  
 990 realistic oceans are inviscid: A link between form stress and bottom pres-  
 991 sure torques. *Journal of Physical Oceanography*, 31(10), 2871–2885. doi:  
 992 10.1175/1520-0485(2001)031<2871:WWBCIR>2.0.CO;2
- 993 Jackson, L., Hughes, C. W., & Williams, R. G. (2006). Topographic control of basin  
 994 and channel flows: The role of bottom pressure torques and friction. *Journal of*  
 995 *Physical Oceanography*, 36(9), 1786–1805. doi: 10.1175/JPO2936.1
- 996 Jagannathan, A., Srinivasan, K., McWilliams, J. C., Molemaker, M. J., & Stew-  
 997 art, A. L. (2021). Boundary layer-mediated vorticity generation in currents  
 998 over sloping bathymetry. *Journal of Physical Oceanography*, 1757–1778. doi:  
 999 10.1175/jpo-d-20-0253.1
- 1000 Large, W. G., & Yeager, S. G. (2009, aug). The global climatology of an interannu-

- 1001 ally varying air - Sea flux data set. *Climate Dynamics*, 33(2-3), 341–364. doi:  
1002 10.1007/s00382-008-0441-3
- 1003 Le Bras, I. A. A., Sonnewald, M., & Toole, J. M. (2019, nov). A barotropic vorticity  
1004 budget for the subtropical north atlantic based on observations. *Journal of*  
1005 *Physical Oceanography*, 49(11), 2781–2797. doi: 10.1175/JPO-D-19-0111.1
- 1006 Le Corre, M., Gula, J., & Tréguier, A. M. (2020). Barotropic vorticity balance of the  
1007 North Atlantic subpolar gyre in an eddy-resolving model. *Ocean Science*. doi:  
1008 10.5194/os-16-451-2020
- 1009 Lemarié, F., Kurian, J., Shchepetkin, A. F., Jeroen Molemaker, M., Colas, F., &  
1010 McWilliams, J. C. (2012). Are there inescapable issues prohibiting the use of  
1011 terrain-following coordinates in climate models? *Ocean Modelling*, 42, 57–79.  
1012 doi: 10.1016/j.ocemod.2011.11.007
- 1013 Lévy, M., Jahn, O., Dutkiewicz, S., Follows, M. J., & D’Ovidio, F. (2015). The dy-  
1014 namical landscape of marine phytoplankton diversity. *Journal of the Royal So-*  
1015 *ciety Interface*. doi: 10.1098/rsif.2015.0481
- 1016 Lévy, M., Klein, P., Tréguier, A. M., Iovino, D., Madec, G., Masson, S., & Taka-  
1017 hashi, K. (2010). Modifications of gyre circulation by sub-mesoscale physics.  
1018 *Ocean Modelling*, 34(1-2), 1–15. doi: 10.1016/j.ocemod.2010.04.001
- 1019 Madec, G., Bourdallé-Badie, R., Chanut, J., Samson, E. C., Coward, A., Ethé,  
1020 C., ... Samson, G. (2019, oct). *NEMO ocean engine*. Zenodo. doi:  
1021 10.5281/zenodo.1464816
- 1022 McDougall, T. J., & Barker, P. M. (2011). Getting started with TEOS-10 and the  
1023 Gibbs Seawater (GSW) oceanographic toolbox. *SCOR/IAPSO WG, 127*, 1–  
1024 28. Retrieved from <https://www.teos-10.org/>
- 1025 Mesinger, F., & Arakawa, A. (1976). Numerical methods used in atmospheric mod-  
1026 els. *GARP Publications Series, 17. Global Atmospheric Research Programme*  
1027 *(GARP)*, 64 pp..
- 1028 Niiler, P. P. (1966, aug). On the theory of wind-driven ocean circulation. *Deep-*  
1029 *Sea Research and Oceanographic Abstracts*, 13(4), 597–606. doi: 10.1016/0011  
1030 -7471(66)90591-2
- 1031 Perezhugin, P. (2019). Deterministic and stochastic parameterizations of ki-  
1032 netic energy backscatter in the NEMO ocean model in Double-Gyre config-  
1033 uration. In *Iop conference series: Earth and environmental science*. doi:  
1034 10.1088/1755-1315/386/1/012025
- 1035 Ruggiero, G. A., Ourmières, Y., Cosme, E., Blum, J., Auroux, D., & Verron, J.  
1036 (2015). Data assimilation experiments using diffusive back-and-forth nudg-  
1037 ing for the NEMO ocean model. *Nonlinear Processes in Geophysics*. doi:  
1038 10.5194/npg-22-233-2015
- 1039 Sadourny, R. (1975). The Dynamics of Finite-Difference Models of the Shallow-  
1040 Water Equations. *Journal of Atmospheric Sciences*, 32(4), 680–689. doi: 10  
1041 .1175/1520-0469(1975)032<0680:TDOFDM>2.0.CO;2
- 1042 Schoonover, J., Dewar, W., Wienders, N., Gula, J., McWilliams, J. C., Mole-  
1043 maker, M. J., ... Yeager, S. (2016). North Atlantic barotropic vorticity  
1044 balances in numerical models. *Journal of Physical Oceanography*. doi:  
1045 10.1175/JPO-D-15-0133.1
- 1046 Song, Y., & Haidvogel, D. (1994). A Semi-implicit Ocean Circulation Model Using  
1047 a Generalized Topography-Following Coordinate System. *Journal of Computa-*  
1048 *tional Physics*, 115(1), 228–244. doi: 10.1006/jcph.1994.1189
- 1049 Stewart, A. L., McWilliams, J. C., & Solodoch, A. (2021). On the Role of Bot-  
1050 tom Pressure Torques in Wind-Driven Gyres. *Journal of Physical Oceanogra-*  
1051 *phy*, 51(5), 1441–1464. doi: 10.1175/jpo-d-20-0147.1
- 1052 Stommel, H. (1948). The westward intensification of wind-driven ocean cur-  
1053 rents. *Eos, Transactions American Geophysical Union*. doi: 10.1029/  
1054 TR029i002p00202
- 1055 Storkey, D., Blaker, A. T., Mathiot, P., Megann, A., Aksenov, Y., Blockley, E. W.,

- 1056 ... Sinha, B. (2018, aug). UK Global Ocean GO6 and GO7: A traceable  
1057 hierarchy of model resolutions. *Geoscientific Model Development*, 11(8), 3187–  
1058 3213. doi: 10.5194/gmd-11-3187-2018
- 1059 Styles, A. F., Bell, M. J., Marshall, D. P., & Storkey, D. (2022). *Data for "Spurious*  
1060 *forces can dominate the vorticity budget of ocean gyres on the C-grid"*. Zenodo.  
1061 doi: 10.5281/zenodo.5513825
- 1062 Vallis, G. K. (2017). Atmospheric and oceanic fluid dynamics: Fundamentals and  
1063 large-scale circulation, second edition. *Atmospheric and Oceanic Fluid Dynam-*  
1064 *ics: Fundamentals and Large-Scale Circulation, Second Edition*, 1–946. doi: 10  
1065 .1017/9781107588417
- 1066 Van Der Walt, S., Schönberger, J. L., Nunez-Iglesias, J., Boulogne, F., Warner,  
1067 J. D., Yager, N., ... Yu, T. (2014, jun). Scikit-image: Image processing in  
1068 python. *PeerJ*, 2014(1), e453. doi: 10.7717/peerj.453
- 1069 Willebrand, J., Barnier, B., Böning, C., Dieterich, C., Killworth, P. D., Le Provost,  
1070 C., ... New, A. L. (2001, jan). Circulation characteristics in three eddy-  
1071 permitting models of the North Atlantic. *Progress in Oceanography*, 48(2-3),  
1072 123–161. doi: 10.1016/S0079-6611(01)00003-9
- 1073 Yeager, S. (2015). Topographic coupling of the atlantic overturning and gyre circula-  
1074 tions. *Journal of Physical Oceanography*. doi: 10.1175/JPO-D-14-0100.1

Figure 1.

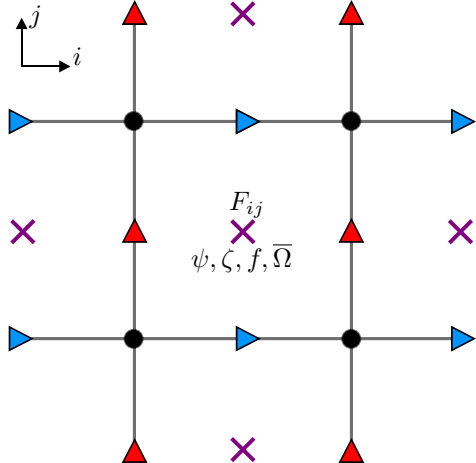
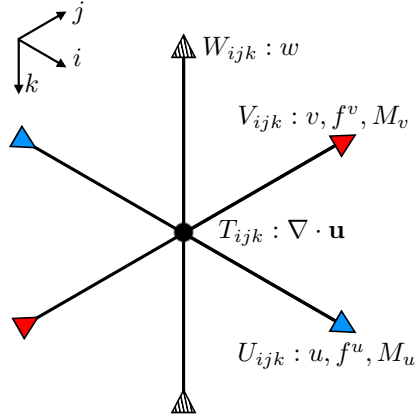
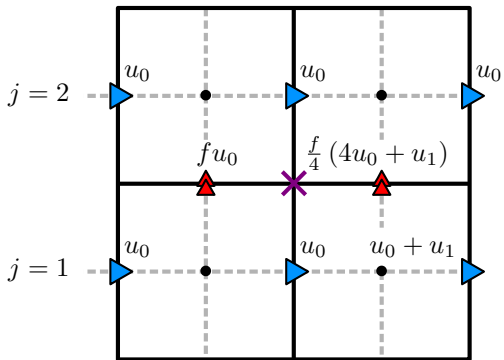
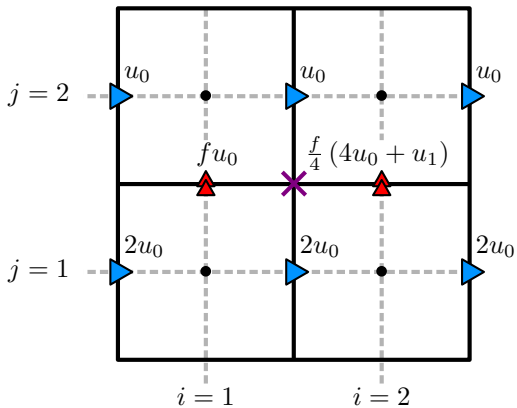


Figure 2.

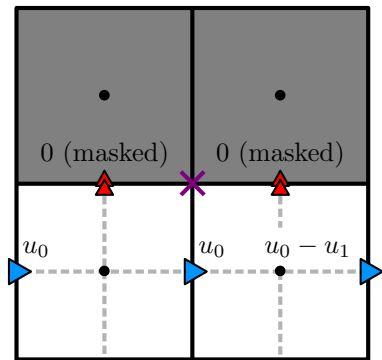
$k = 1$  (Upper)



Depth-integrated fields /  $\Delta z$



$k = 2$  (Lower)



Depth-integrated fields /  $\Delta z$

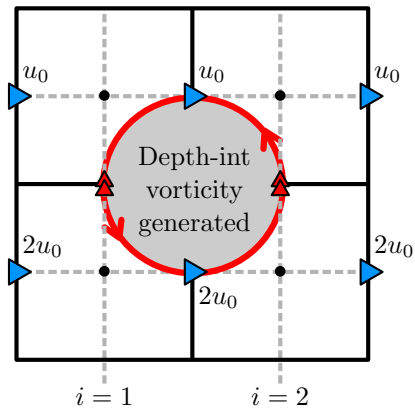
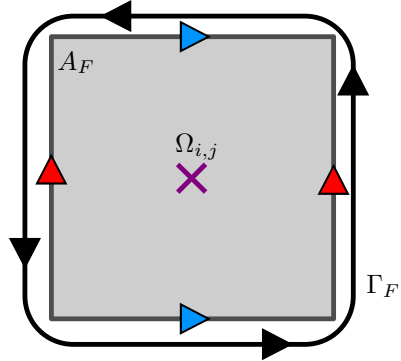
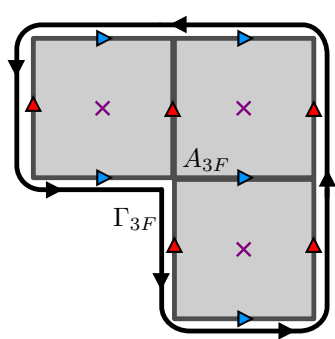


Figure 3.



$$\Omega_{i,j} = \frac{1}{A_F} \iint_{A_F} \nabla \times \mathbf{M} \cdot \hat{\mathbf{k}} dA$$

$$\Omega_{i,j} = \frac{1}{A_F} \oint_{\Gamma_F} \mathbf{M} \cdot d\mathbf{l}$$



$$I_{3F} = \iint_{A_{3F}} \nabla \times \mathbf{M} \cdot \hat{\mathbf{k}} dA$$

$$I_{3F} = \oint_{\Gamma_{3F}} \mathbf{M} \cdot d\mathbf{l}$$

Figure 4.

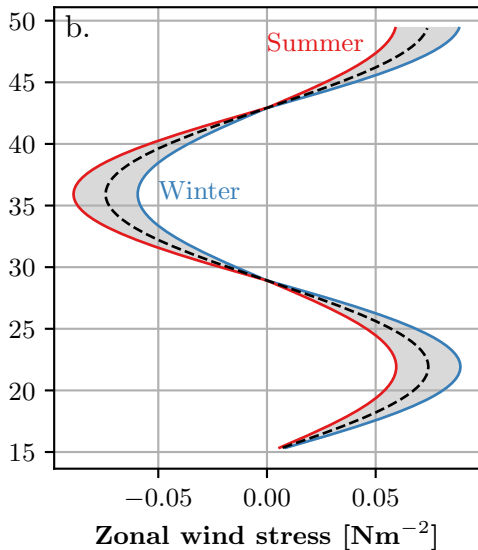
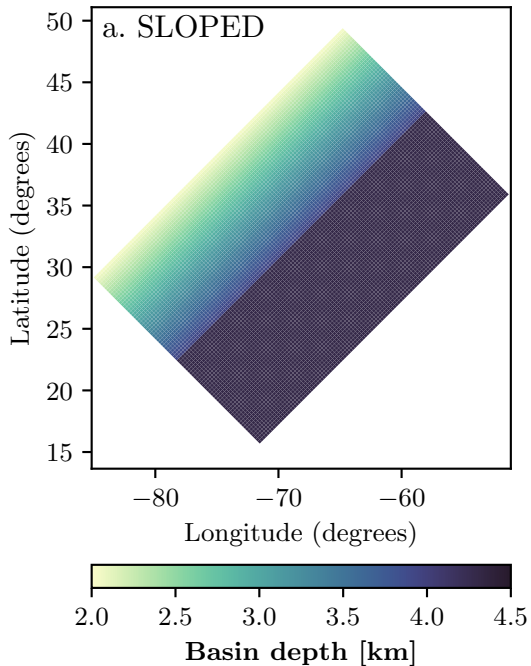


Figure 5.

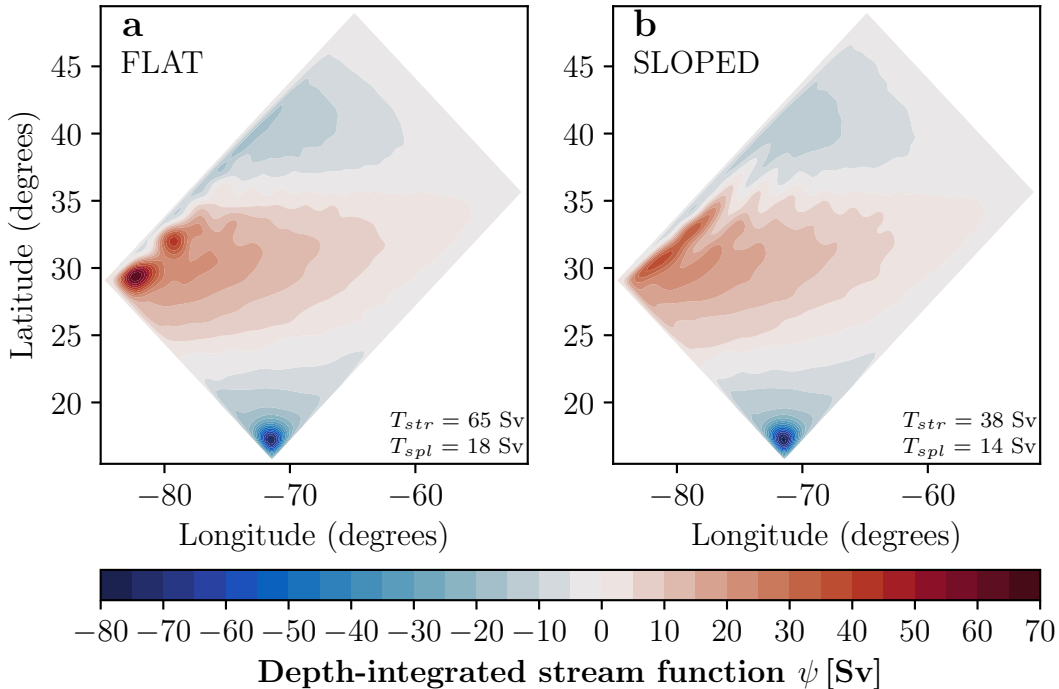


Figure 6.

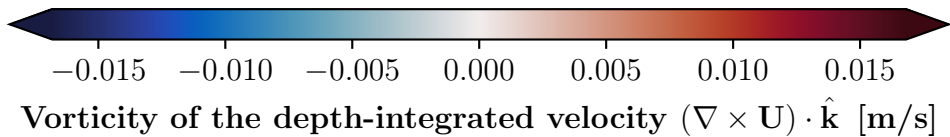
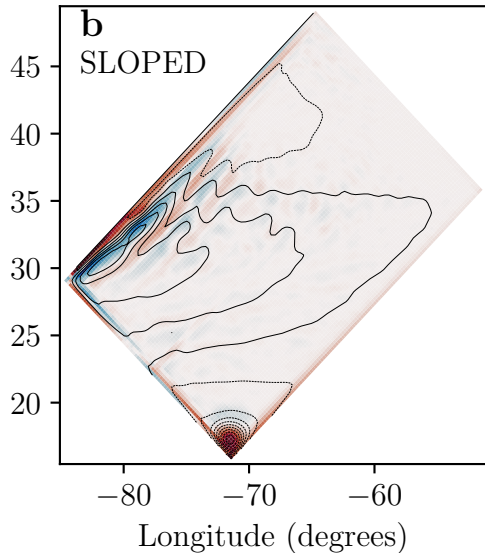
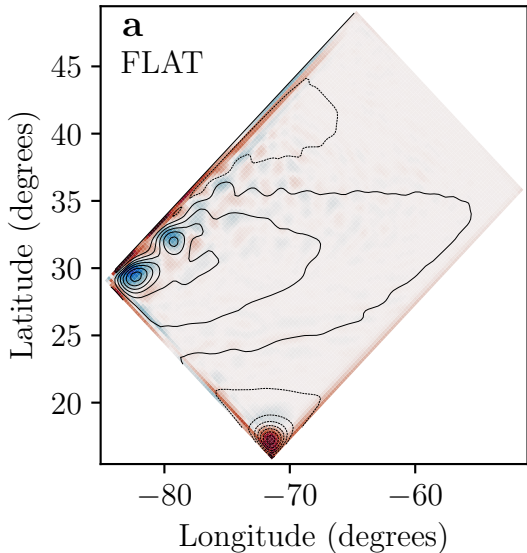


Figure 7.

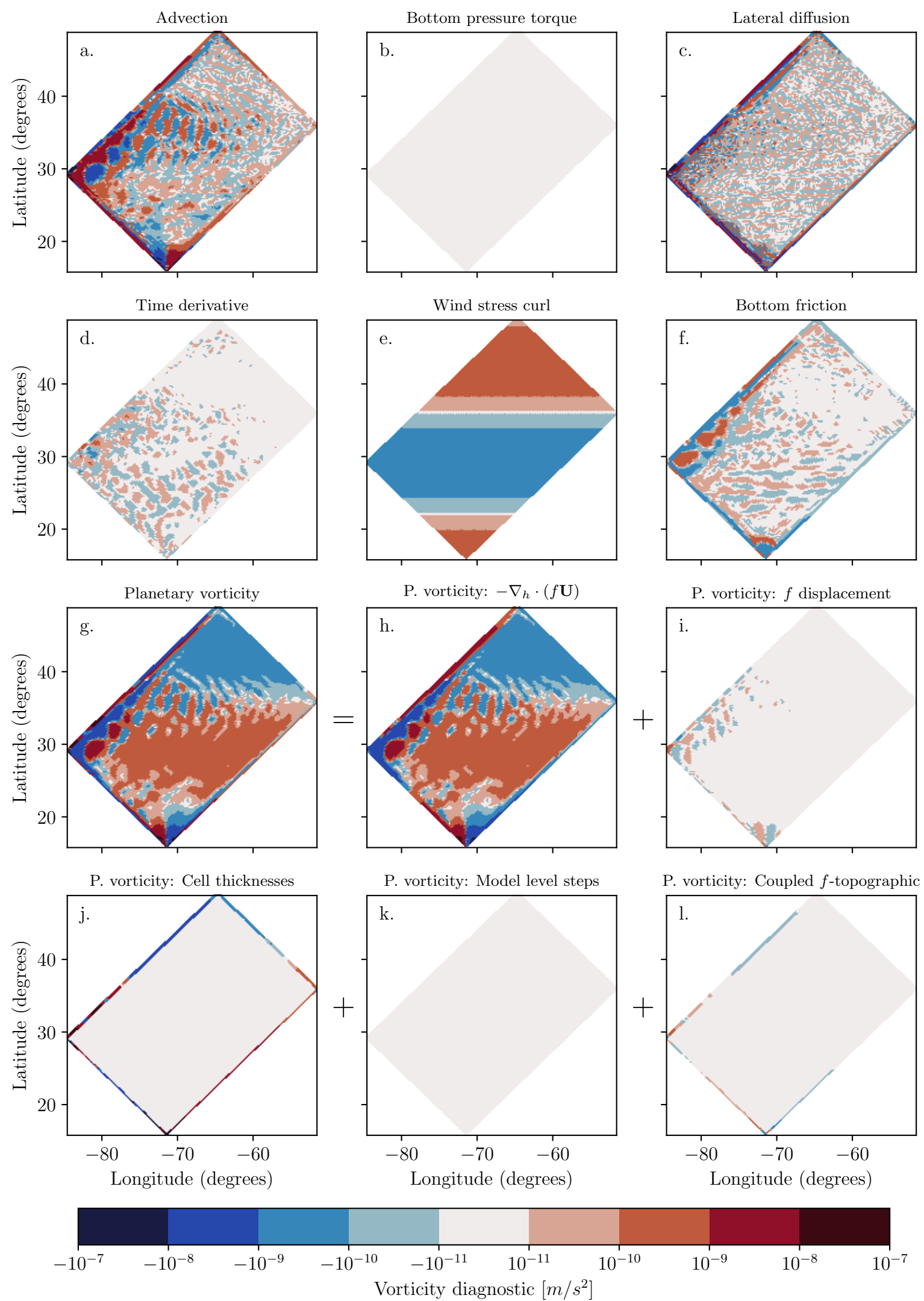


Figure 8.

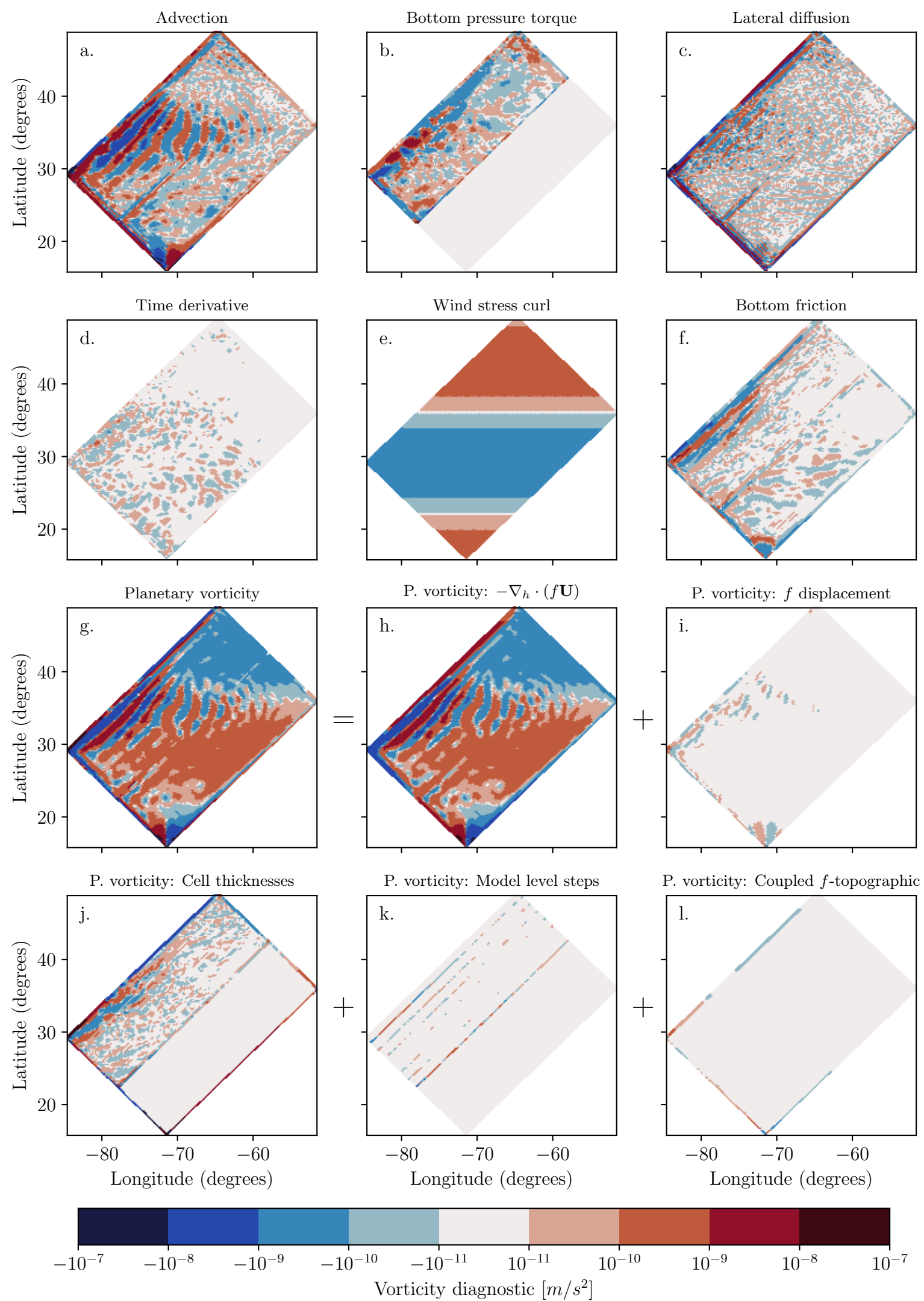
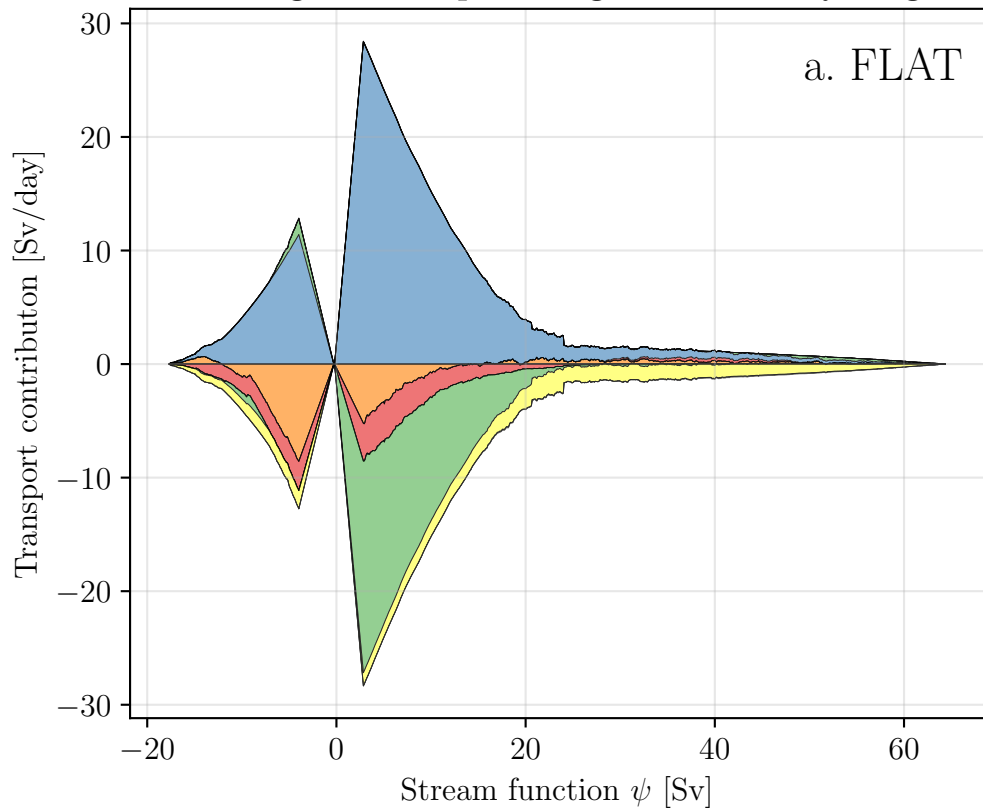
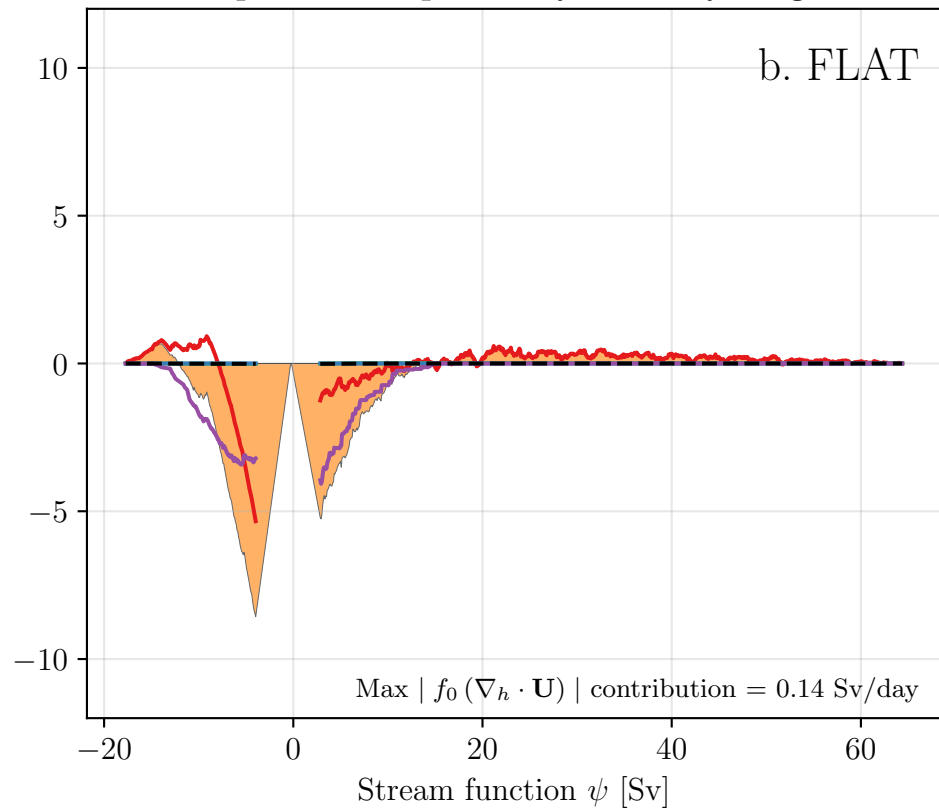


Figure 9.

Contour integrals of depth-integrated vorticity diagnostics



Decomposition of planetary vorticity diagnostic



Example contours

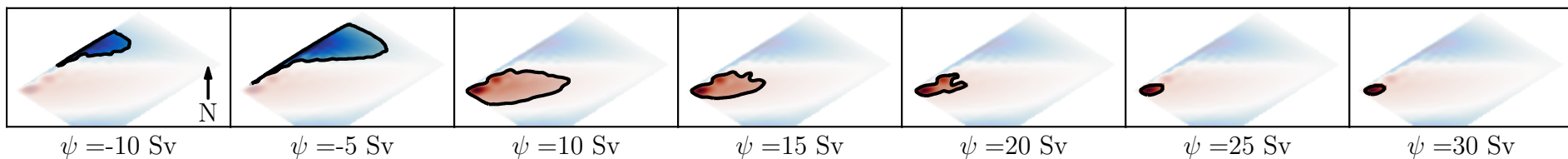
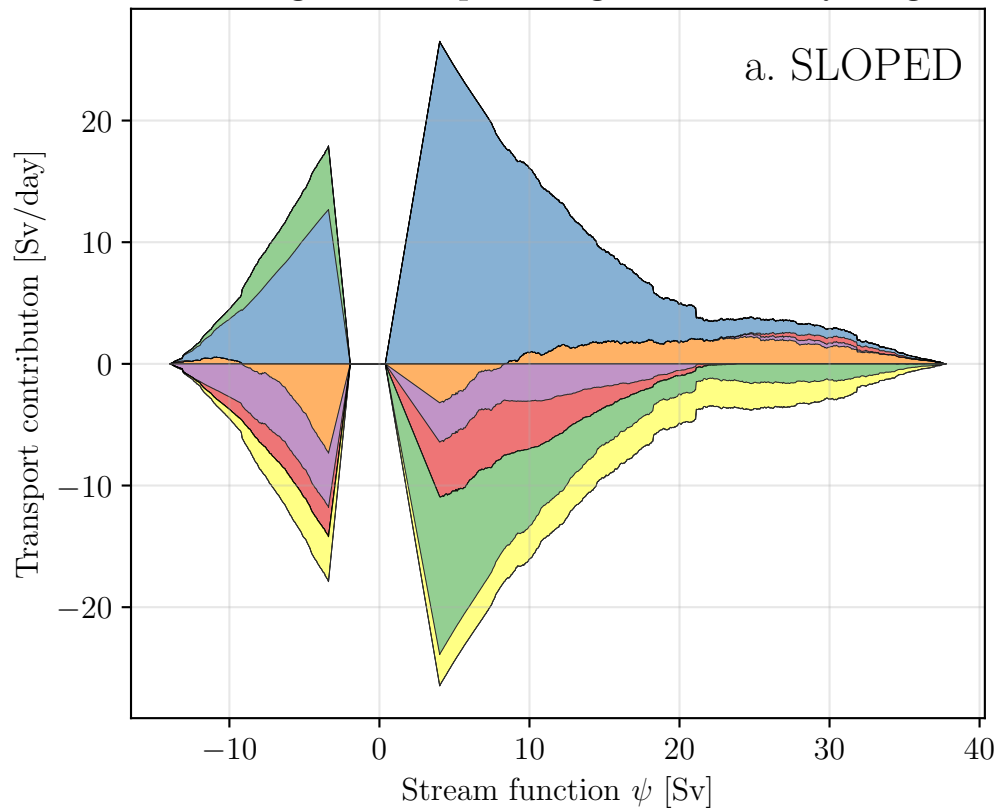
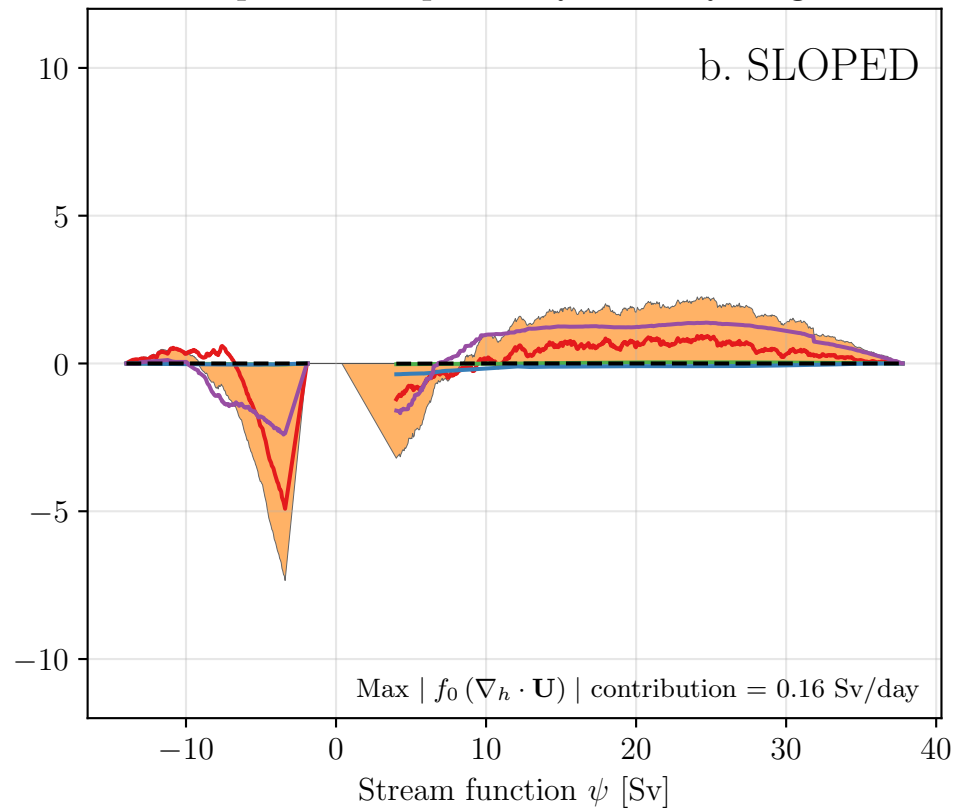


Figure 10.

Contour integrals of depth-integrated vorticity diagnostics



Decomposition of planetary vorticity diagnostic



Example contours

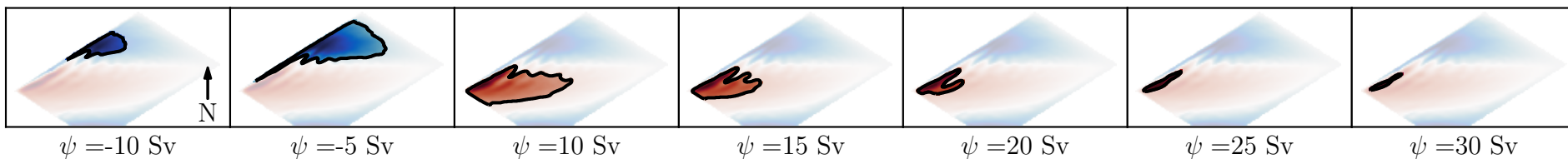


Figure 11.

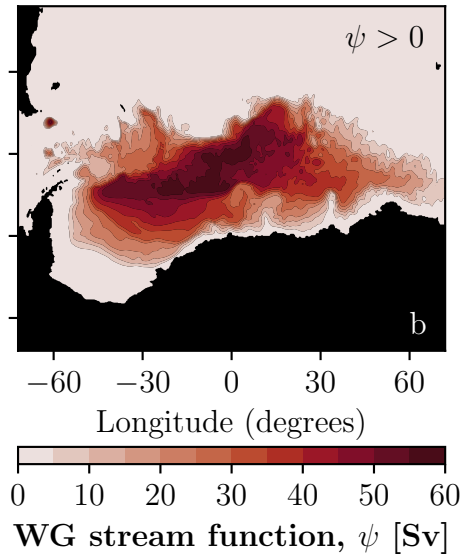
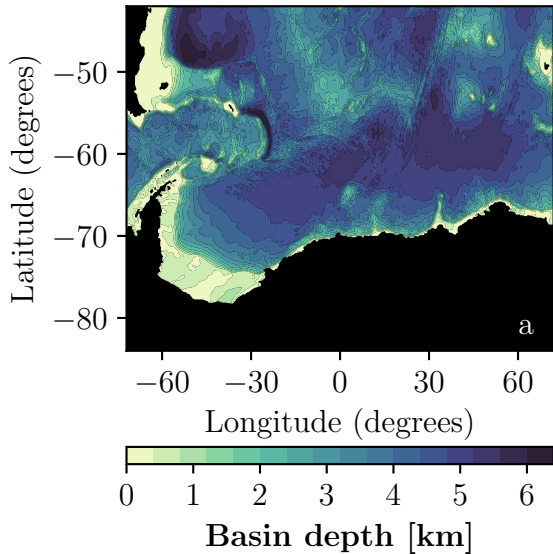
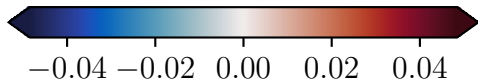
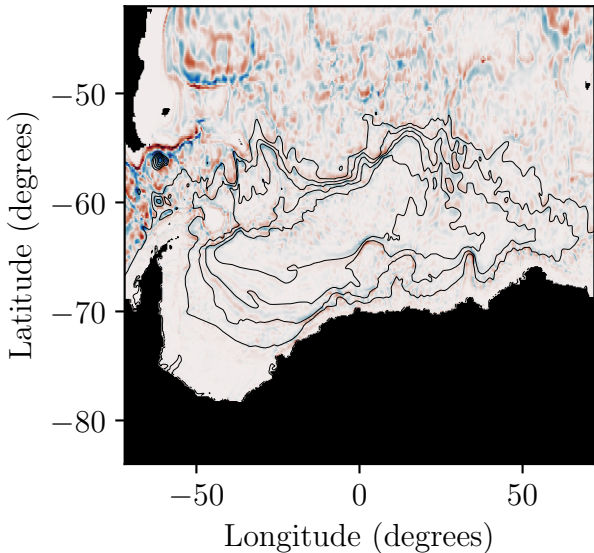


Figure 12.



Vorticity of the depth-integrated velocity  $(\nabla \times \mathbf{U}) \cdot \hat{\mathbf{k}}$  [m/s]

Figure 13.

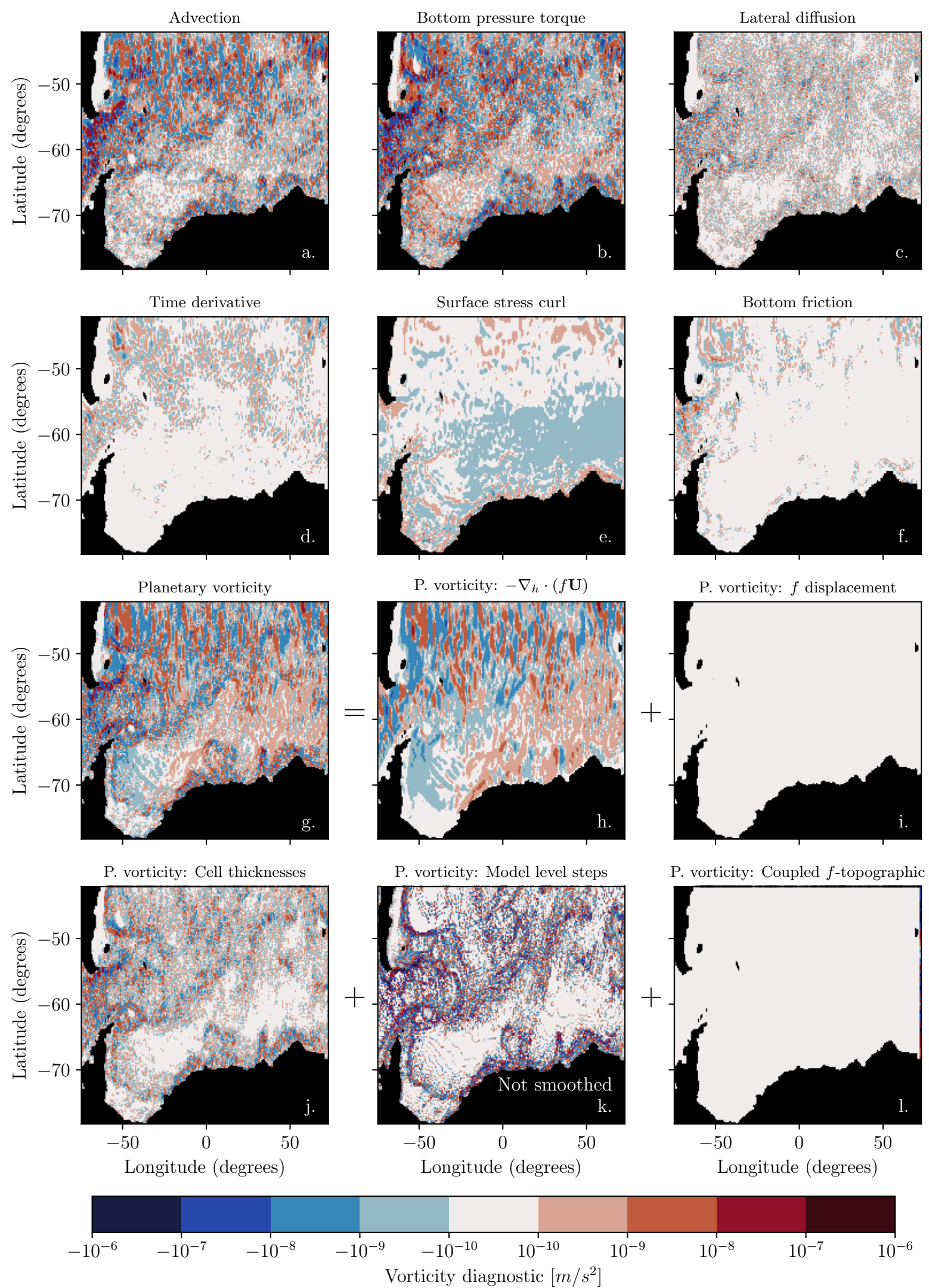
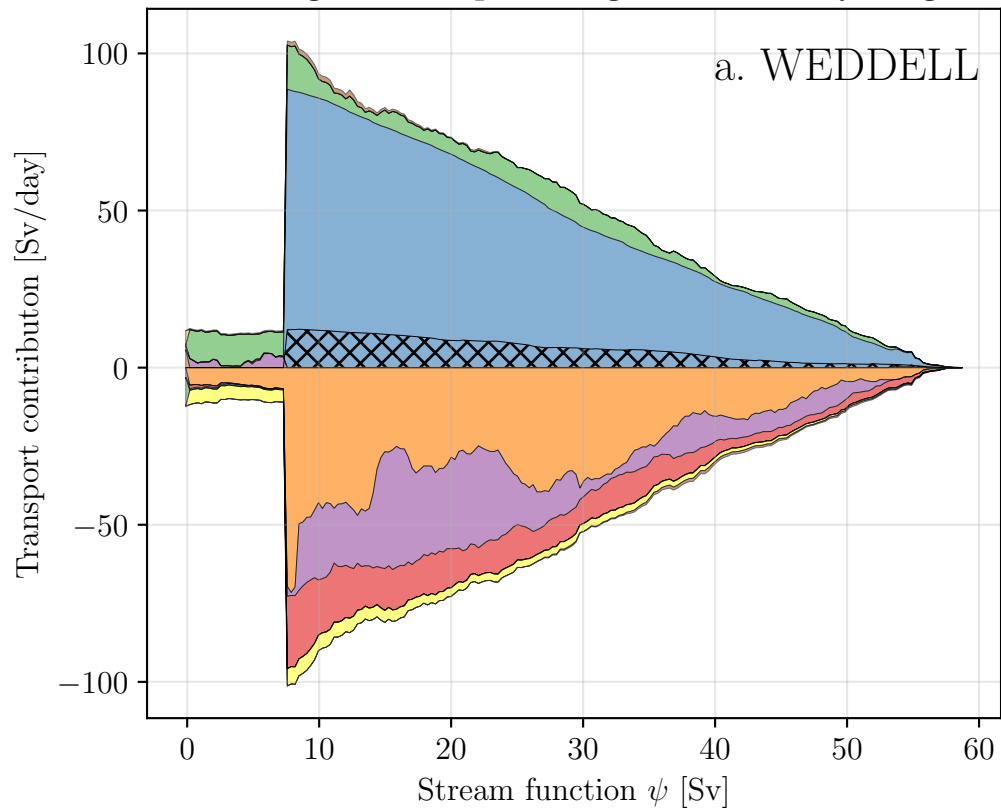
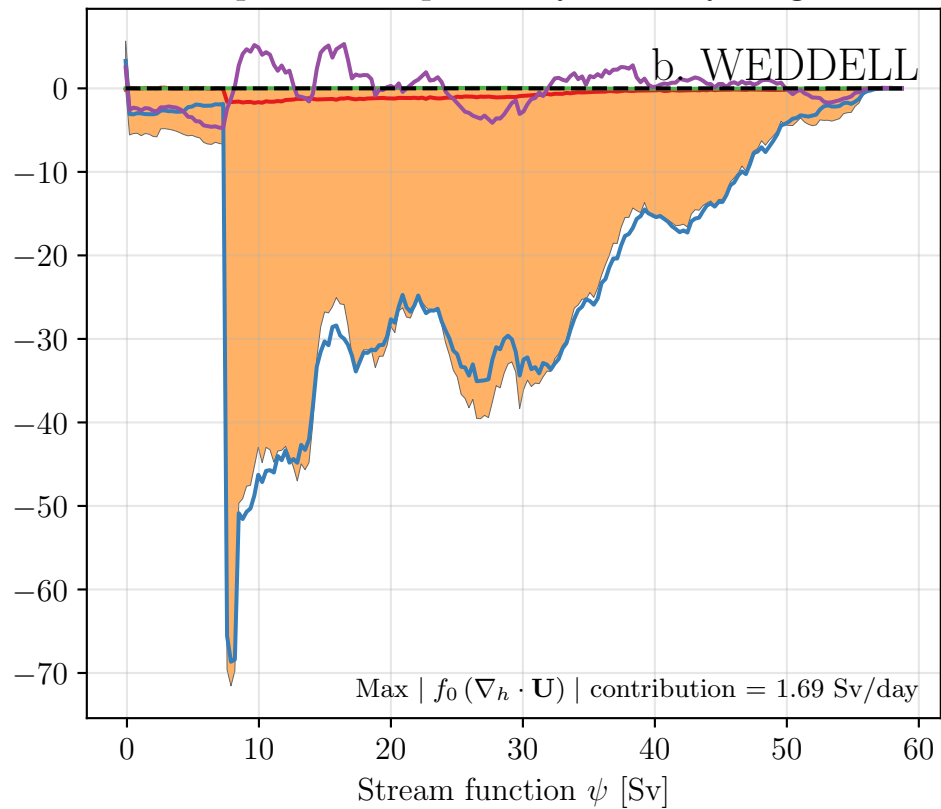


Figure 14.

Contour integrals of depth-integrated vorticity diagnostics



Decomposition of planetary vorticity diagnostic



Example contours

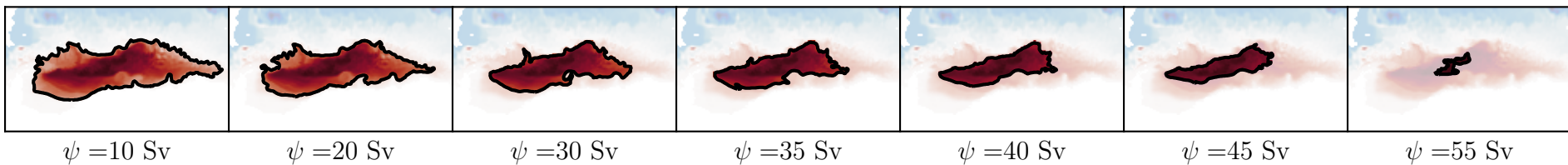
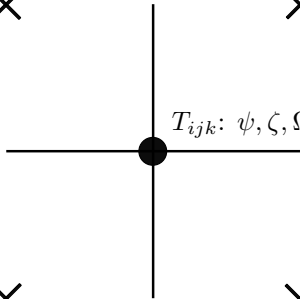


Figure 15.



$V_{ijk}: u, v, M_u, M_v, f_{ij}$



Tracer point ( $T$ )



Vector point ( $V$ )

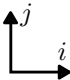
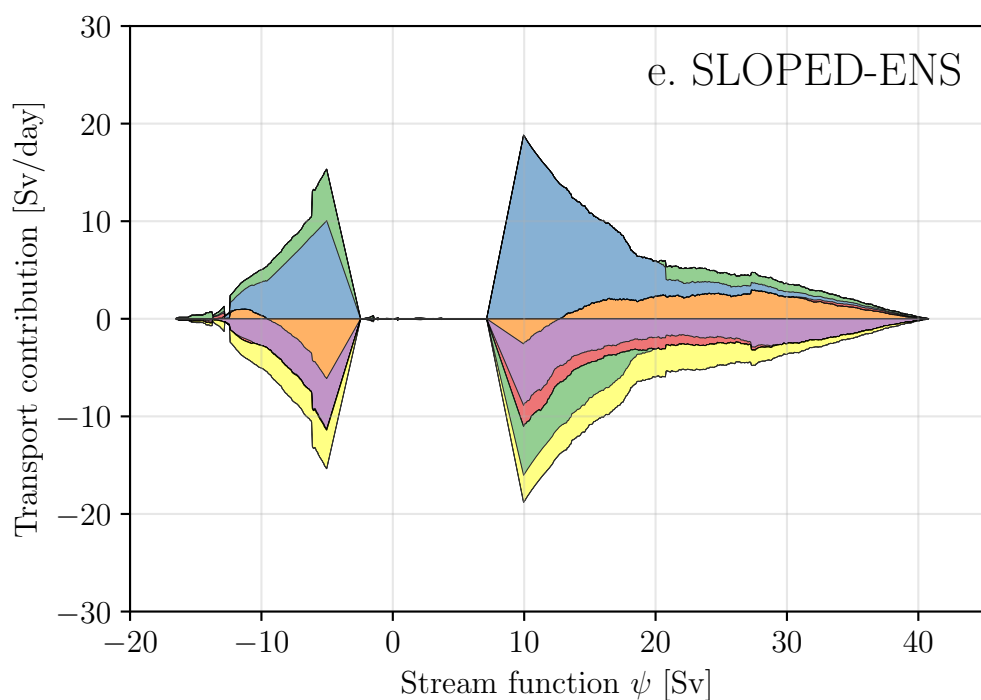
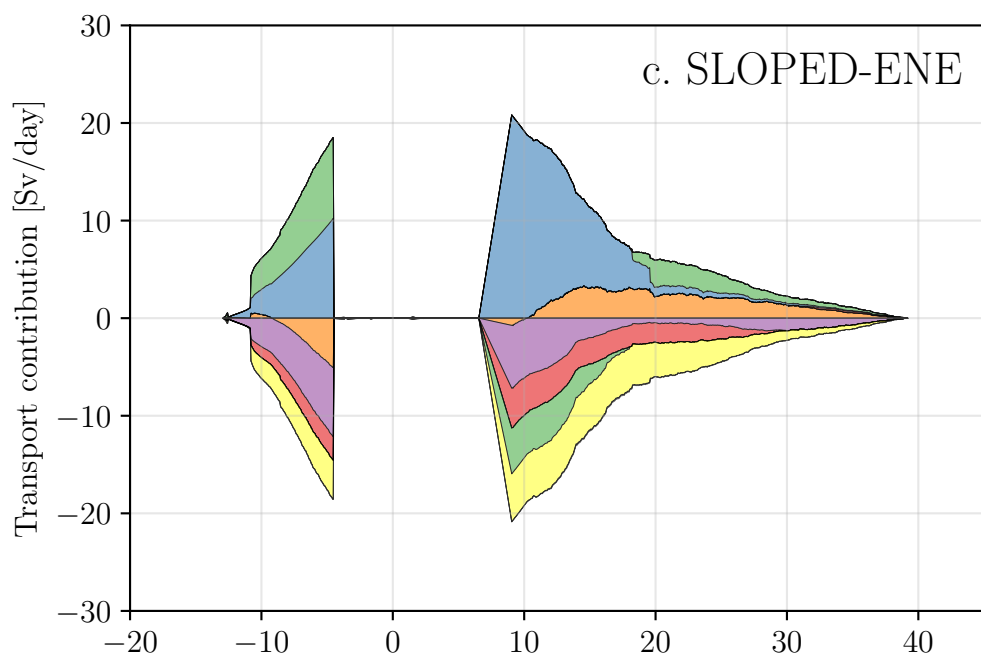
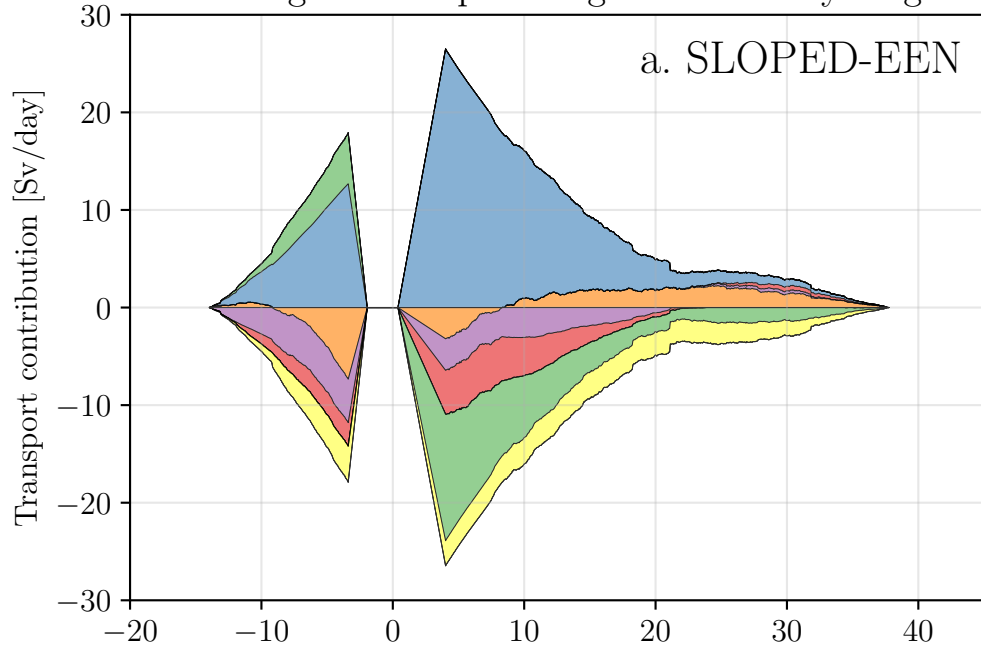


Figure C1.

Contour integrals of depth-integrated vorticity diagnostics



Decomposition of planetary vorticity diagnostic

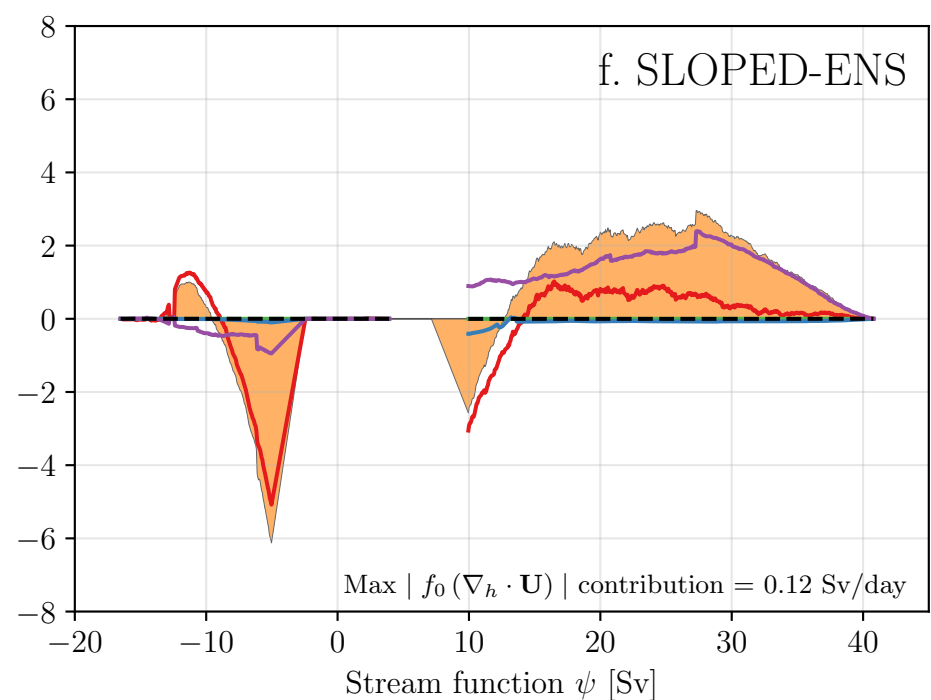
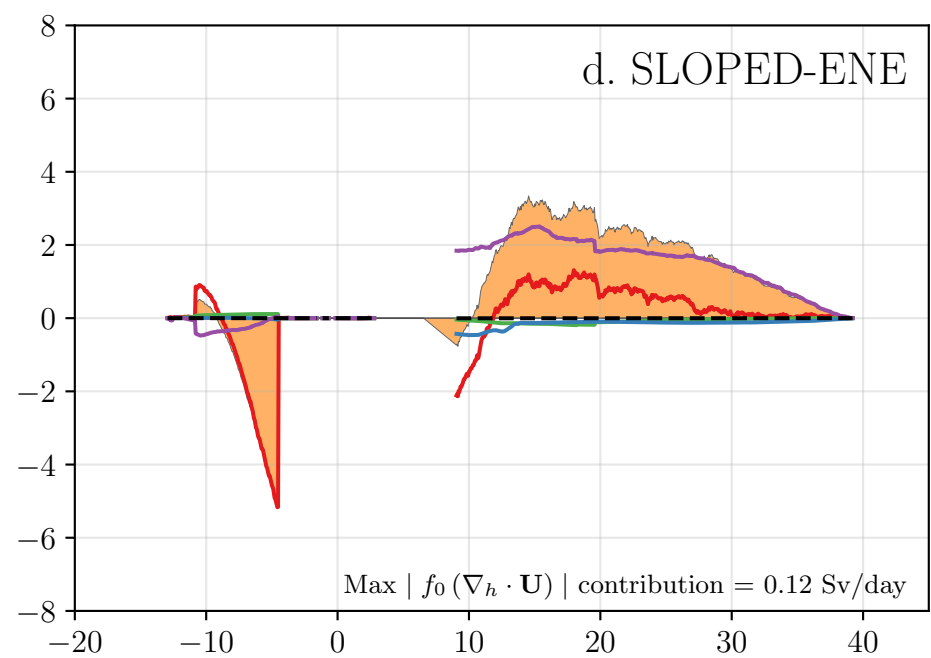
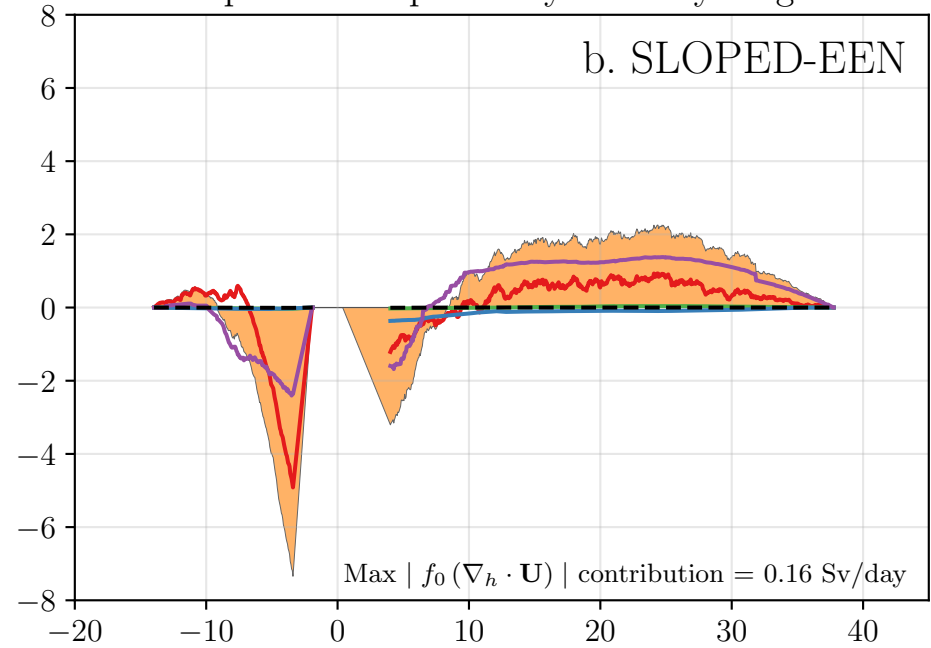
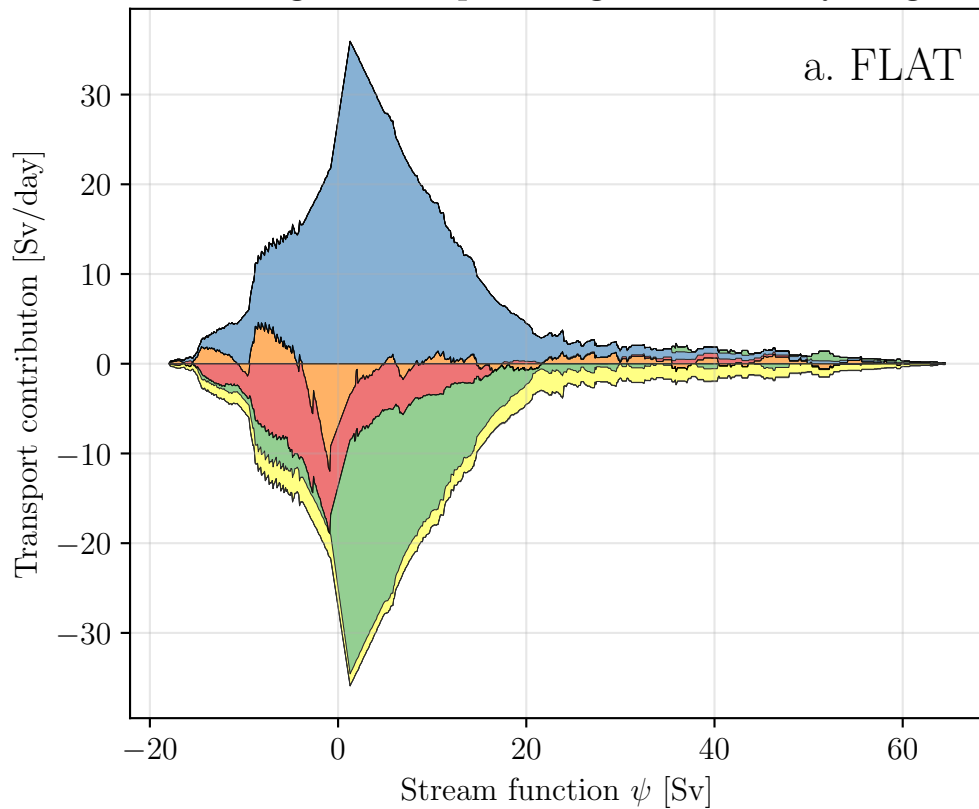
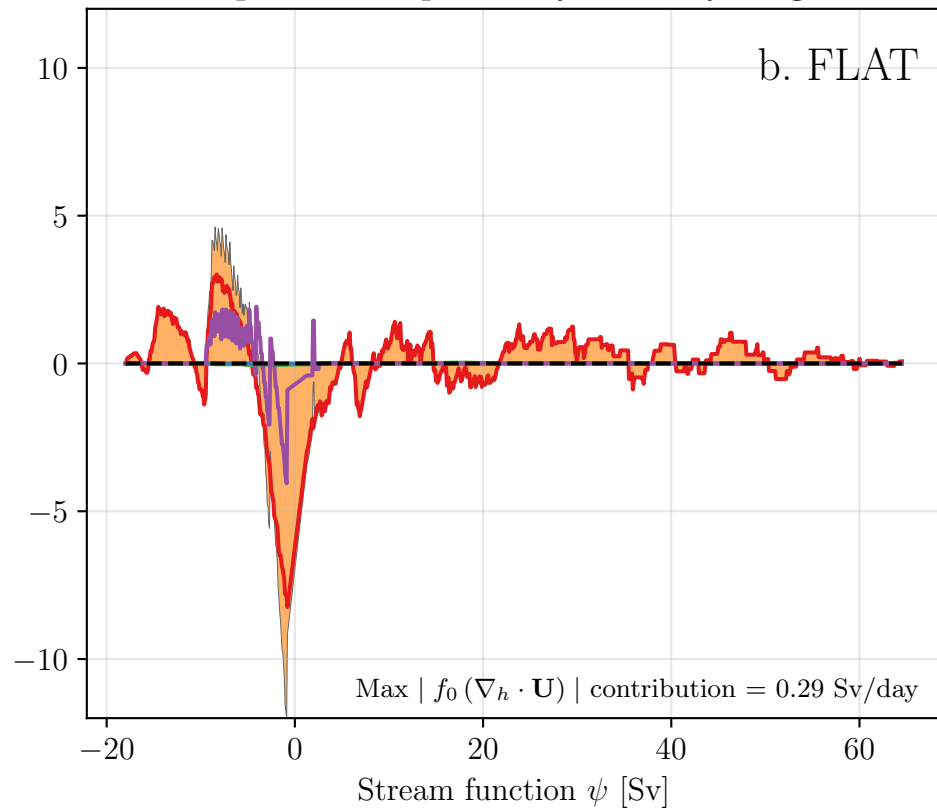


Figure D1.

Contour integrals of depth-integrated vorticity diagnostics



Decomposition of planetary vorticity diagnostic



Example contours

